How does salinity shape ocean circulation and ice geometry on Enceladus and other icy satellites?

Wanying Kang[a,1]**, Tushar Mittal**[a]**, Suyash Bire**[a]**, Jean-Michel Campin**[a]**, and John Marshall**[a]

[a]Earth, Atmospheric and Planetary Science Department, Massachusetts Institute of Technology

Of profound astrobiological interest, Enceladus appears to have a global subsurface ocean that is salty, indicating water-rock reaction at present or in the past, important for its habitability. Here, we investigate how salinity affects ocean dynamics and equilibrium ice shell geometry and use knowledge of Enceladus' contemporary ice shell geometry and tidal heating rates to help constrain ocean salinity. Assuming steady state conditions, we show that the meridional overturning circulation of the ocean, driven by heat and salt exchange with the ice, has opposing signs at very low and very high salinities. Regardless of these differing circulations, heat and freshwater converge toward the equator, where the ice is thick, acting to homogenize thickness variations. In order to maintain the observed ice thickness variation, ocean heat convergence cannot overwhelm well-constrained heat loss rates through the thick equatorial ice sheet. This requirement is found to be violated if the ocean is very fresh or very salty, or if the main heat source is in the core rather than the ice shell. Instead, if the ocean on Enceladus has a salinity of intermediate range – 10 to 20 g/kg or so – the temperature- and salinity-induced density gradient largely cancel one another, leading to much reduced overturning and equatorial heat convergence rates and consistent budgets.

Enceladus | icy moon | planetary science

Since the Cassini and Galileo mission, Enceladus (a satellite of Saturn) and Europa (a satellite of Jupiter) have been revealed to have a high astrobiological potential, satisfying all three necessary conditions for life: 1) the presence of liquid water (1, 2), 2) a source of energy (3, 4), and 3) a suitable mix of chemical elements (1, 5–10). In particular, the geyser-like sprays ejected from the fissures over Enceladus's south pole (11–13) provide a unique opportunity to understand the chemistry and dynamics of Enceladus' interior without landing on and drilling through a typically 20km-thick ice shell. Within the geyser samples collected by Cassini, CO_2, methane (5), sodium salt (1), hydrogen (7), and macromolecular organic compounds (8) have been found. This suggests a chemically active environment able to sustain life (9, 10). However, to make optimum use of these samples to infer the chemical environment of the subsurface ocean, one needs to better understand tracer transport by the interior ocean and hence ocean circulation itself.

Ocean circulation on Enceladus is driven by heat and salinity fluxes from both the silicate core (3) and the ice shell (4, 14, 15). The partition of heat production between the ice and the silicate core has a direct control over ocean dynamics. Moreover ocean salinity plays a key role since it determines whether density decreases or increases with temperature (16) (see Fig.1c). For example if the ocean is very fresh then heat released by hydrothermal vents will not trigger penetrative convection from below. Furthermore, the global scale circulation of a salty ocean could be completely different from that in a fresh ocean, as has been explored in Earth's ocean (17).

Despite its importance, the salinity of Enceladus' ocean remains uncertain. Calculations of thermochemical equilibria over a range of hydrothermal and freezing conditions for chondritic compositions, suggest a salinity ranging between 2-20 psu (g/kg), with a higher likelihood of it being below 10 psu (18–20). However, at least 17 psu is required to keep the geysers' liquid–gas interface convectively active to ensure that they do not freeze up (21). Sodium-enriched samples taken from south pole sprays by Cassini have a salinity of 5-20 psu. This can be considered a lower bound since the interaction of cold water vapor sprays with their environment is likely to lower the salinity of droplets through condensation (1). This is also uncertain, however, since fractional crystallization and disequilibrium chemistry may partition components in such a way that geyser particles are not directly representative of the underlying ocean (22). Furthermore, if particles originate from a hydrothermal vent, composition can also deviate far from that of the overall ocean (3, 20). In a separate line of argument, the size of silica nano-particles carried along in the sprays suggests a salinity < 40 psu, but this is sensitive to assumptions about ocean pH and the dynamics of hydrothermal vents (6).

An additional complication is that the heat partition between Enceladus' ice shell and silicate core is under debate. The largest source of uncertainty stems from the assumed rheology of both the ice shell and the silicate core to which the rates and patterns of tidal heat generation are sensitive. Hydrogen and nanometre-sized silica particles have been detected on Enceladus, providing clear geochemical evidence for active seafloor venting (6, 7). However, whether this submarine hydrothermalism is the dominant heat source preventing the ocean from freezing remains inconclusive due to our limited understanding of the core's rheology (3, 23). Another potential heat source is the tidal dissipation within the ice. While the ice geometry on top of the ocean is qualitatively consistent with heating primarily in the ice

shell (24), present dynamical models of ice are unable to reproduce enough heat to maintain such a thin ice shell (4, 25). Attempts to account for higher heat generation through use of more advanced models of ice rheology have thus far not been successful (4, 14, 25–29).

Given the above uncertainties, here we use our understanding of ocean dynamics to provide further constraints on ocean salinity and the partition of heating between the ice shell and the core. To do this we make use of observations of ice shell geometry to provide boundary conditions for ocean circulation and model the ocean circulation driven by them as a function of salinity and tidal heating partitions. Some lead to heat transports which are consistent with what is known about tidal heating rates, others do not, enabling us to discriminate between them.

1. Boundary conditions on ocean circulation

Data provided by Cassini has enabled reconstructions to be made of Enceladus' ice thickness variations (24, 30–33). The solid curve in Fig.1b show the zonal mean ice thickness deduced by *Hemingway & Mittal 2019* (24). Thick ice at the equator with a poleward thinning trend is notable. The thinnest ice shell over the south pole is only a fifth as thick as the equatorial ice shell. Such ice thickness variations have two effects. First, thick equatorial ice creates high pressure depressing the local freezing point leading to a roughly -0.1 K temperature anomaly just beneath the ice compared to the poles (solid curve in Fig.1b). Second, thickness variations will drive ice to flow from thick-ice regions to thin-ice regions on million-year time-scales (34–36). To compensate the smoothing effect of the ice flow, ice must form in low latitudes and melt in high latitudes. Assuming an ice rheology, we can calculate ice flow speeds using an upside-down shallow ice model (details are given in the SM section 1D). In this way, we can infer the required freezing/melting rate, as shown by the dashed curve in Fig.1b. This freezing and melting will lead to a meridional salinity gradient over time via brine rejection and fresh water input which, in steady state, must be balanced by salinity transport in the ocean.

The combined effect of these temperature and salinity gradients just beneath the ice will be to make equatorial waters saltier and colder than polar waters. In a salty ocean, where water volume contracts when it is cold (known as the beta ocean), we expect the ocean to sink at the cold low latitudes, because the water density is high there (see Fig. 2b). In contrast, in a fresh ocean (known as the alpha ocean), the opposite is possible because of seawater's anomalous expansion upon cooling (see Fig. 2a). Thus the overturning circulation in alpha and beta oceans can be expected to be of opposite sign. However, no matter in which direction the ocean circulates, heat will be converged toward the equator, because of the tendency of cold equatorial water and warm polar water to mix together. Limited by the efficiency of conductive heat loss through the thick equatorial ice, the equatorward heat convergence cannot be arbitrarily strong. By examining the heat budget of the ice, then, knowledge of ocean heat transport under various salinities and core-shell heat partitions can be used to discriminate between different scenarios.

In order to study the possible ocean circulation and heat transport on Enceladus in this way, we set up a zonally-averaged ocean circulation model to sweep across a range of mean salinities ($S_0 = 4$, 7, 10, 15, 20, 25, 30, 35 and 40 psu) and core-shell heat partitions (0-100%, 100-0% and 20-80%). Our model has its ocean covered by an ice shell that resembles that of the present-day Enceladus (24) (solid curve in Fig.1b), which is assumed to be sustained against the ice flow by a prescribed freezing/melting q (gray dashed curve in Fig.1b). By prescribing q, we cut off the positive feedback loop between the ocean heat transport and the ice freezing/melting rates, ensuring that the circulation will always be consistent with those freshwater fluxes. When heat production by the silicate core is assumed to be non-zero, an upward heat flux at the bottom is prescribed. Guided by models of tidal heating described in SM, this is assumed to be slightly polar-amplified (see purple curve in Fig.1d). At the water-ice interface, a downward salinity flux $S_0 q$ is imposed to represent the brine rejection and freshwater production associated with

Significance Statement

Since the Cassini and Galileo mission, icy ocean worlds such as Enceladus and Europa have become some of the most interesting astrobiological targets in the solar system. This motivates us to explore ocean circulation and transport pathways from the silicate core, where life may thrive, to the ice shell, where we can probe. One key factor that has yet to be explored is the role of ocean salinity in setting the circulation. Salinity determines whether water will expand or contract upon warming near the freezing point, controlling ocean circulation and tracer/heat transport, and shaping ice shell geometry. Understanding such connections may allow us to constrain the salinity of icy moons using the observed ice shell geometry or vice versa.

[1]To whom correspondence should be addressed. E-mail: wanying@mit.edu

Kang *et al.*

freezing/melting. Meanwhile, the ocean temperature there is relaxed toward the local freezing point. Thus the ocean will deposit heat to the ice when its temperature is slightly higher than the freezing point, and vice versa. In order for the heat budget of the ice to close, this ocean-ice heat exchange $\mathcal{H}_{\text{ocn}}$, together with the tidal heat produced in the ice $\mathcal{H}_{\text{ice}}$ (red curve in Fig. 1d) and the latent heat released $\mathcal{H}_{\text{latent}}$ ($\mathcal{H}_{\text{latent}} = \rho L_f q$, where ρ and L_f are the density and fusion energy of ice, see the gray curve in Fig. 1d) should balance the conductive heat loss through the ice shell $\mathcal{H}_{\text{cond}}$ (green curve in Fig. 1d). The degree to which this heat budget is in balance informs us of the plausibility of the assumed salinity and heat partition.[*]

Before going on to describe our results, we emphasize that we have adopted a zonally-averaged modeling framework so that we can readily explore parameter space whilst integrating our models out to an equilibrium state, which takes about 10,000 model years. This necessarily implies that our ocean model is highly parameterized – as are the models of tidal heating and ice flows that are used to provide the forcing at the boundaries that drive it – and so have many unavoidable uncertainties. In particular, and as described in detail in SM and just as in terrestrial ocean models, processes such as convection, diapycnal mixing and baroclinic instability are parameterized guided by our knowledge of the mechanisms that underlie them.
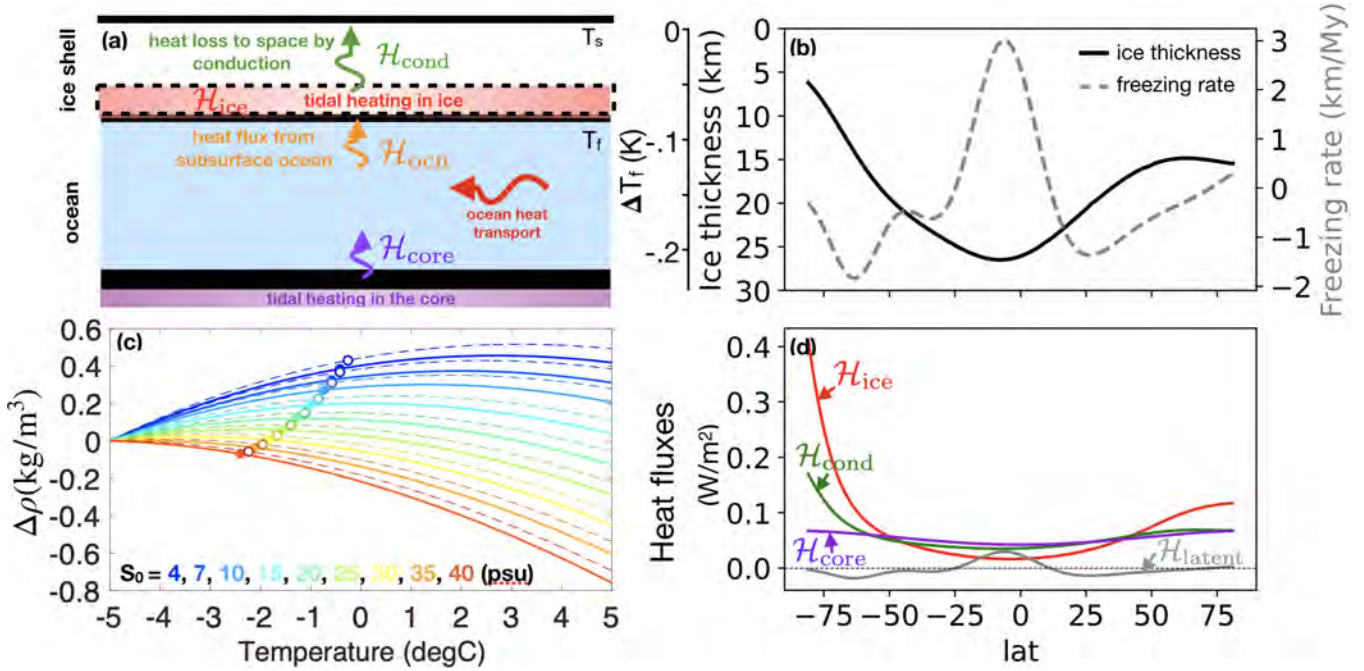
Fig. 1. Panel (a) presents the primary sources of heat and heat fluxes in an icy moon which include: heating due to tidal dissipation in the ice $\mathcal{H}_{\text{ice}}$ and the silicate core $\mathcal{H}_{\text{core}}$, the heat flux from the ocean to the ice $\mathcal{H}_{\text{ocn}}$ and the conductive heat loss to space $\mathcal{H}_{\text{cond}}$. Ocean heat transport is shown by the horizontal arrow. Panel (b) shows the observed ice shell thickness of Enceladus based on shape and gravity measurements (24) (black solid curve, left y-axis). The suppression of the freezing point of water by these thickness variations, relative to that at zero-pressure, is indicated by the outer left y-axis. The gray dashed curve shows the freezing (positive) and melting rate (negative) required to maintain a steady state based on an upside-down shallow ice flow model (y-axis on the right). Panel (c) shows how the density anomaly of water varies as its temperature varies around -5°C as a function of salinity. Moving from cold to warm colors denotes increasing salinity, as indicated by the colored lettering. The solid (dashed) curves are computed assuming the pressure under the 26.5 km (5.6 km) of ice at the equator (south pole). The freezing points are marked by the circles. Panel (d) shown typical magnitudes and profiles of $\mathcal{H}_{\text{ice}}$, $\mathcal{H}_{\text{core}}$, $\mathcal{H}_{\text{cond}}$ and $\mathcal{H}_{\text{latent}}$. The models of heat fluxes and ice flow on which all these curves are based can be found in section 1D of the SM.

2. Patterns of ocean circulation, temperature and salinity

Due to the relatively low freezing point (Fig. 1c) and elevated freezing rate (Fig. 1b) of low latitudes, water just under the ice is colder and saltier than near the poles, regardless of the mean salinity. This pole-to-equator temperature and salinity contrast leads to variations in density, which in turn drive ocean circulation. In Fig. 3(c,e), we present the density anomaly, $\rho_0(\alpha_T \theta' + \beta_S S')$, and the meridional overturning streamfunction $\Psi(\phi, z) = \int_{-D}^{z} \rho(\phi, z') V(\phi, z') \times (2\pi(a - z')\cos\phi)\, dz'$. Here, θ' and S' (plotted in Fig. 3a,b) are the deviation in potential temperature and salinity

---

[*]The global heat budget is closed by design, i.e., $\overline{\mathcal{H}_{\text{cond}}} = \overline{\mathcal{H}_{\text{ice}}} + \overline{\mathcal{H}_{\text{core}}}$. Latent heat's global average vanishes, because $\overline{q} = \overline{\nabla \cdot \mathcal{Q}} = 0$, where $\mathcal{Q}$ is the ice flow.
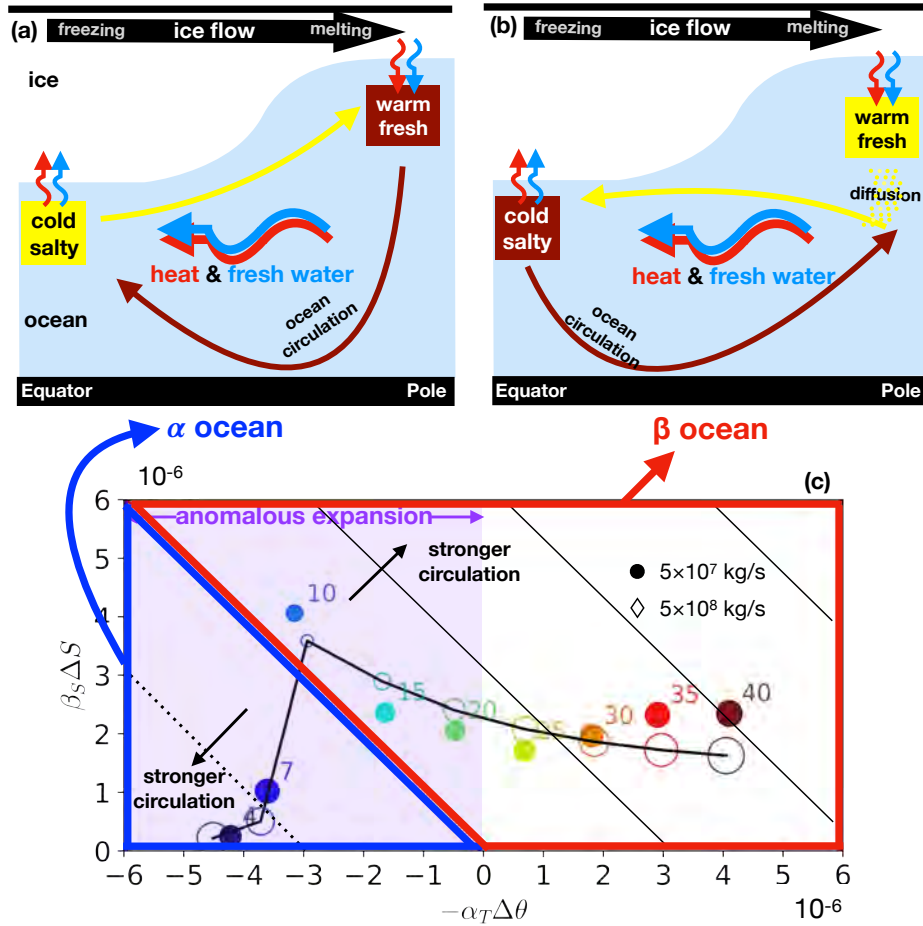
Fig. 2. At the top we show schematics of ocean circulation and associated transports of heat (red wiggly arrows) and fresh water (blue wiggly arrows) for (a) the fresh alpha ocean and (b) the salty beta ocean. Dark brown arrows denote sinking of dense water, light yellow arrows denote rising of buoyant water. The circulations are forced by the freezing/melting required to counterbalance the down-gradient ice flow (thick black arrows marked at the top) and by variations in the freezing point of water due to pressure, as presented in Fig.1b. In panel (c), we present a regime diagram inspired by explicit solutions such as those presented in Fig.3, showing the influence of temperature and salinity anomalies on density as a function of mean salinity, and how the overturning circulation of the ocean responds. Horizontal and vertical axes are the temperature and salinity induced density anomalies at the equator, relative to the north pole. Note that both ΔS and $-\Delta T$ are positive (the equator is always saltier and colder than the pole), and the sign of the coordinates reflect the sign of α_T and β_S: β_S is always positive, but α_T increases from negative to positive as S_0 increases. In the high/low S_0 experiments, the signs of $-\alpha_T\Delta T$ and $\beta_S\Delta S$ are the same/opposite. Red (blue) solid lines delineate the β ocean (α ocean) regimes, in which the density is dominated by salinity (temperature) anomalies respectively, as set out in the schematics above. Purple shading highlights the regime where anomalous expansion of seawater is present with negative α_T so that warming leads to sinking. The position of key ocean model experiments in this space is represented by the symbols. The number on the shoulder of each circle gives the S_0 used in that experiment. The size of each circle represents the amplitude of the overturning circulation (the peak Ψ occurs in the northern hemisphere). The 45° tilted black lines are isolines of the equator-to-pole density difference $\Delta\rho$. Solid lines denote dense water near the equator and dotted lines denote dense water over the poles. As illustrated by the black arrows, circulation strengthens with $\Delta\rho$ moving away from the transition line between α ocean and β ocean. The empty circles connected by a black solid curve show the fit of the conceptual model developed in Section 4 which broadly captures the behavior of the explicit calculation using our full model.

from the reference, α_T and β_S are the thermal expansion and haline contraction coefficient, V is the meridional current, ρ is the water density, and D is the ocean depth, ϕ denote latitude and z points upwards.

Since the density gradient induced by temperature variations can either enhance or diminish that induced by salinity, depending on the mean salinity S_0, the overturning circulation can run in either direction. When S_0 is greater than 22 psu, water expands with increasing temperature ($\alpha_T > 0$, see reddish curves in Fig.1c). As a result, the cold and salty water under the thick equatorial ice shell is denser than polar waters, as shown in Fig.3-c3 and sketched in Fig. 2b using the dark brown color. Equatorial waters therefore sink, as shown in Fig.3-e3 (indicated in Fig.2b using the dark brown arrow). This circulation pattern broadly agrees with that suggested by *Lobo et al. 2021* (37) using a diagnostic ocean model.

However, when S_0 is below 22 psu, the thermal expansion coefficient changes sign ($\alpha_T < 0$, as shown by the bluish curves in Fig.1c). This so-called anomalous expansion of water results in the temperature-induced density difference and the salinity-induced density difference partially cancelling one another, giving rise to two possibilities. If the salinity factor dominates (β ocean), the overturning circulation becomes one of sinking at the equator, as show in Fig.3-e2 and sketched in Fig.2b using a dark brown arrow. But if temperature dominates (α ocean), the overturning circulation flips direction with sinking over the poles (Fig.3-e1 and Fig.2a) because water is denser there (Fig.3-c1). The switch in the sense of the overturning circulation with salinity can also occur in models of Earth's ocean (17), even though Earth's ocean is forced rather differently.

The transition from polar to equatorial sinking is governed by the density difference between the poles and the equator. Taking the north pole as a reference, the temperature-related density anomaly at the equator can be written as $-\alpha_T \Delta\theta$, and the salinity-related density anomaly as $\beta_S \Delta S$, where $\Delta\theta$ and ΔS are the potential temperature and salinity anomaly at the equator relative to the north pole. Fig.2c presents the strength of the overturning circulation from all nine experiments in the $(-\alpha_T \Delta T, \ \beta_S \Delta S)$ space: the size of the circles are proportional to Ψ. The 45 degree tilted line denotes perfect cancellation between the saline and temperature-driven overturning circulations: it passes between 7 psu and 10 psu, explaining why these two experiments have the weakest circulation compared to all others. On moving away from this line in either direction the strength of the overturning circulation increases but is of opposite sign, as represented schematically in the schema above.

The sense of the overturning circulation shapes the tracer patterns and associated zonal currents. Downwelling regions (low latitudes for a salty ocean and high latitudes for a fresh ocean) advect density, temperature and salinity anomalies, set at the ocean-ice interface, into the interior ocean. Note the bending of the temperature and salinity contours equatorward (poleward) when downwelling occurs at the poles (equator), as shown in Fig. 3. This results in meridional density gradients which are in a generalized[†] thermal wind balance with zonal currents (Fig. 3d). When the meridional density gradients are weak, the zonal flow is weak, overturning circulation is weak, and the temperature and salinity contours are mostly vertical (see the second column of Fig. 3).

3. Implication of ocean heat transport for the heat budget of the ice shell

Irrespective of the sense of the vertical overturning circulation of the ocean, warm polar water is mixed equatorward and the cold equatorial water mixed poleward. This results in heat convergence toward the equator for all salinities (see Fig. 4a). This in turn would tend to flatten ice thickness variations (a manifestation of the ice pump mechanism (38)). Although ocean heat transport is always equatorward, its amplitude co-varies with the circulation strength. As can be seen in Fig. 4a, the heat convergence in an ocean with an intermediate salinity is a small fraction of that in the end-member cases. Such sensitivity is unsurprising because the heat flux is proportional to the product of the overturning strength multiplied by a temperature contrast (39): the latter is broadly the same in all experiments but the former strongly depends on the mean salinity [‡]. Another common feature of the meridional heat transport profiles is that heat is transported across the equator into the southern hemisphere where the ice is thinner than in the northern hemisphere. The amplitude ranges from a few to a few 10's of GW, depending on the strength of the overturning circulation, a significant fraction of the 35GW of heating being generated by the tide. If this southward heat transport pattern were to also exists when the ocean is fully coupled to the ice, it will provide a mechanism to induce hemispheric symmetry breaking of the ice thickness, in addition to the ice-rheology feedback proposed by *Kang & Flierl 2020* (40).

From the meridional heat transport, we can compute $\mathcal{H}_{\rm ocn}$, the heat flux transmitted from the ocean to the ice [§],

---

[†] The terms associated with the horizontal component of Coriolis force must be included.

[‡] The coldest and warmest locations are adjacent to the water-ice interface whose temperature is set by the local freezing point of water, meridional variation of which is dominated by pressure effects which are the same in all experiments: see Eq.6 in the SM where the dependence of freezing point on salinity and pressure is explicitly set out.

[§] $\mathcal{H}_{\rm ocn}$ was calculated in two ways. First, we directly diagnosed the heat exchange between ice and ocean. Secondly we calculated the meridional heat flux convergence (Fig.4a) and added the bottom heat flux to it (Eq.8 in the SM). They yield identical results, indicating that the ocean was in equilibrium.
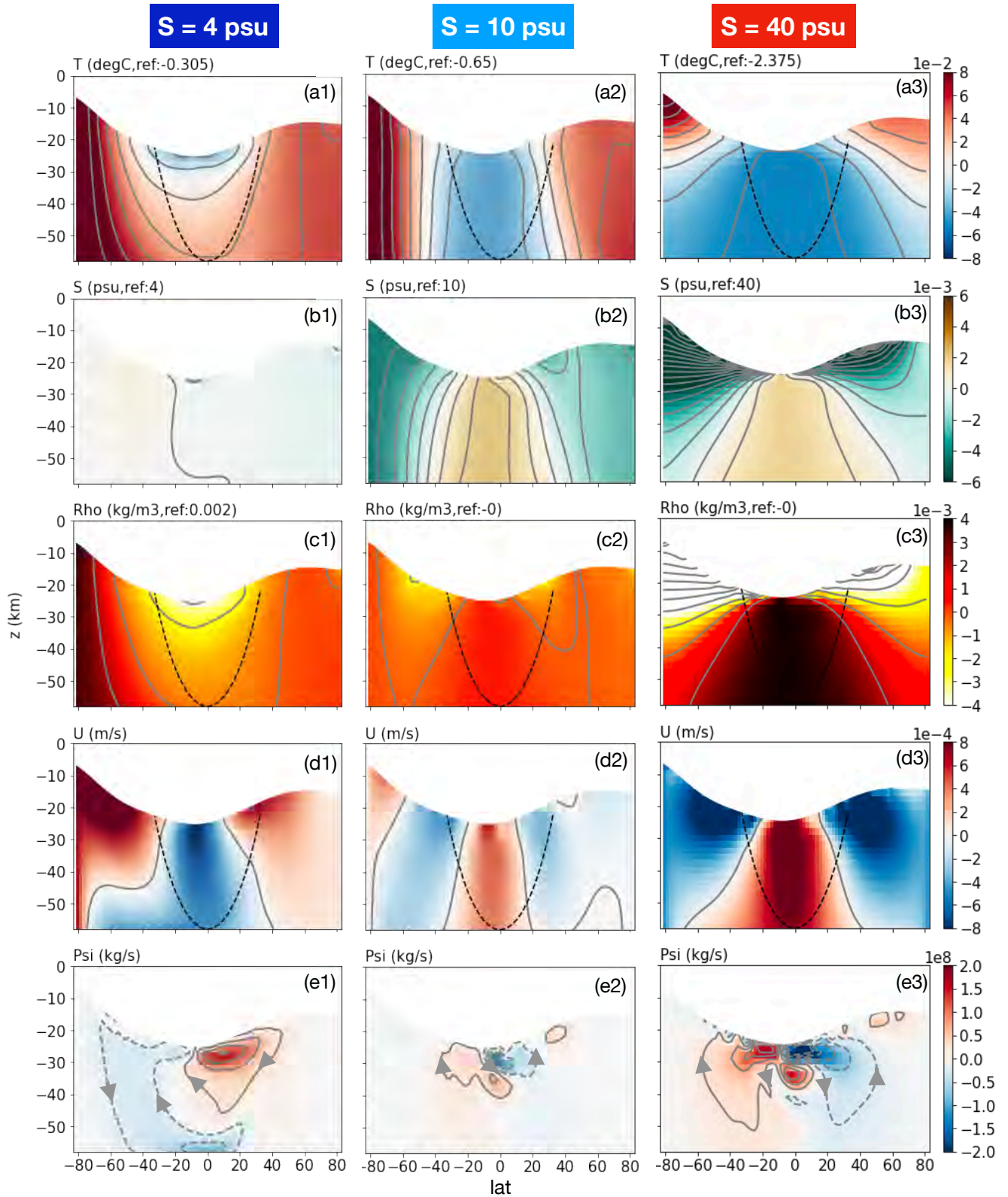
Fig. 3. Ocean circulation and thermodynamic state for experiments driven by the glacial melt and under-ice temperature distributions shown in Fig. 1b for oceans with various mean salinities. Moving from top to bottom present temperature T, salinity S, density anomaly $\Delta\rho$, zonal flow speed U and meridional overturning streamfunction Ψ with arrows indicating the sense of flow. The left column presents results for a low salinity ocean ($S_0 = 4$ psu), the right column for high salinity ($S_0 = 40$ psu), and the middle column for an ocean with intermediate salinity ($S_0 = 10$ psu). The reference temperature and salinity (marked at the top of each plot) are subtracted from T and S to better reveal spatial patterns. Positive U indicates flow to the east and positive Ψ indicates a clockwise overturning circulation. Black dashed lines mark the position of the tangent cylinder.

and diagnose how much tidal heating is required to close the heat budget of the ice,

$$\hat{\mathcal{H}}_{\text{ice}} = \mathcal{H}_{\text{cond}} - \mathcal{H}_{\text{ocn}} - \rho_i L_f q. \tag{1}$$

The $\hat{\mathcal{H}}_{\text{ice}}$ inferred from our suite of ocean solutions is shown by the solid curves in Fig.4b. For comparison, we also present the predicted tidal heating $\mathcal{H}_{\text{ice}}$ given by a tidal dissipation model (details of the model can be found in section 1E of the SM) in the same figure using black dashed curves – this curve is also plotted in Fig.1d. We see that for many salinities (very fresh and very salty), the implied tidal heating is actually large and negative!, which is obviously not physically possible.

To quantify the mismatch between $\hat{\mathcal{H}}_{\text{ice}}$ and $\mathcal{H}_{\text{ice}}$, we introduce an index (plotted as the solid curve in Fig.4c),

$$I_{\text{mis}} = \overline{\left(\frac{\hat{\mathcal{H}}_{\text{ice}} - \mathcal{H}_{\text{ice}}}{\max\{\mathcal{H}_{\text{ice}}, 20 \text{ mW/m}^2\}} \right)}, \tag{2}$$

where the over-bar represents a global area-weighted average. The max function in the denominator helps avoid the singularity when $\mathcal{H}_{\text{ice}} \to 0$.

Those ocean solutions with a strong overturning circulation (e.g., $S_0 = 4$, 40 psu) focus a large amount of heat to low latitudes, introducing a heat budget discrepancy as large as 100 mW/m^2[¶], which is reflected by the large I_{mis}. As noted above, near the equator, the inferred $\hat{\mathcal{H}}_{\text{ice}}$ even becomes significantly negative, conflicting with the positive definite nature of tidal dissipation. The best match is achieved in the $S_0 = 10$ psu scenario (Fig. 4c). In such an intermediate salinity regime, the temperature and salinity-induced density anomalies almost cancel one-another out (see Fig.2c), the overturning circulation is weak (Fig.3-e2), and the heat convergence is broadly consistent with tidal heating rates.

It is interesting to note that the increase in the mismatch is steeper on the fresh side of 10 psu than the salty side (Fig.4c). This is related to the different energetics of ocean circulation in an α vs a β-ocean. As pointed out by *Zeng & Jansen 2021* (41), in an α ocean, the buoyancy gain at the equator is deeper in the water column than the buoyancy loss at the poles and ocean circulation can always be energized against friction since dense polar water higher up the water column is transported to depth. However, in a β ocean, the opposite is true and equatorial dense water cannot easily be drawn upward to the polar ice shell without extra energy input by diffusion (42). This difference can be seen in Fig.3-e. The overturning circulation in an α ocean (Fig.3-e1) can directly connect the water-ice interface at the pole to equatorial regions; in contrast in a β ocean (Fig.3-e3), the circulation weakens moving poleward and almost completely vanishes in the fresh water lens formed under the polar ice shell. Strong stratification develops in the diffusive layer (Fig.3-c3) which sustains an upward buoyancy flux without strong circulation, as indicated in the schematic diagram Fig.2b.

Assuming that some heat generation occurs in the core does not change the overall picture: circulation patterns, temperature/salinity profiles, and meridional heat transport remain broadly similar, as can be seen from Fig. 4(d,e), Fig.S3 and Fig.S4. This is because the heating-induced bottom-to-top temperature difference is typically only a few tens of milliKelvin[‖], much smaller than the equator-to-pole temperature difference induced by the freezing point variations (Fig.3) which is order 0.1 Kelvin — see Fig.1b,c. However, the predicted tidal heating rates in the ice shell approach zero as the core becomes the dominant heat source. As a result, the equatorward ocean heat transport can no longer be effectively compensated by polar-amplified dissipation in the ice shell, and the discrepancy in the heat budget increases. I_{mis} for the 20% core-heating scenario is plotted with a dashed line marked by crosses in Fig. 4c and that for the 100% core-heating scenario plotted in Fig. 4f. In particular, over the south pole where the ice shell is thin, heat is transported equatorward by ocean circulation implying that polar ice will accumulate over time in the absence of local heating within the ice (black dashed curved in panel e). We also observe that for the pure core-heating scenario, the best-matching salinity shifts to 15-20 psu. More detailed discussions of the bottom heating solutions can be found in section 2A of the SM.

To explore sensitivity to parameter choices, we carried out many sets of experiments changing the assumed ice rheology and mixing rates in the ocean. By default, the melting point ice viscosity η_m is set to 10^{14} Pa·s, an intermediate choice between an estimated lower bound of 10^{13} Pa·s and an upper bound of 10^{15} Pa·s (34). In the ice rheology sensitivity test, we let $\eta_m = 2 \times 10^{13}$ Pa·s. Such a lower ice viscosity induces stronger ice flows, which require a greater balancing freezing/melting rate. This in turn enhances the salinity flux imposed upon the ocean, giving rise to larger salinity gradients. Compensating the density anomaly implied by this salinity gradient thus requires a more negative α_T and lower S_0. As shown by the plus signs in Fig. 4c, the best matching S_0 is indeed reduced from 10 psu to 7 psu (the full solution is summarized in Fig.S9 of the SM).

[¶] If used to melt ice, this heat will induce a melting rate of 9.31 km/Myr near the equator, which is twice as strong as the tendency implied by viscous ice flow (shown in Fig. 1b).

[‖] The vertical temperature gradient induced by bottom heating is larger in a fresh ocean because of the suppression of convection gets.
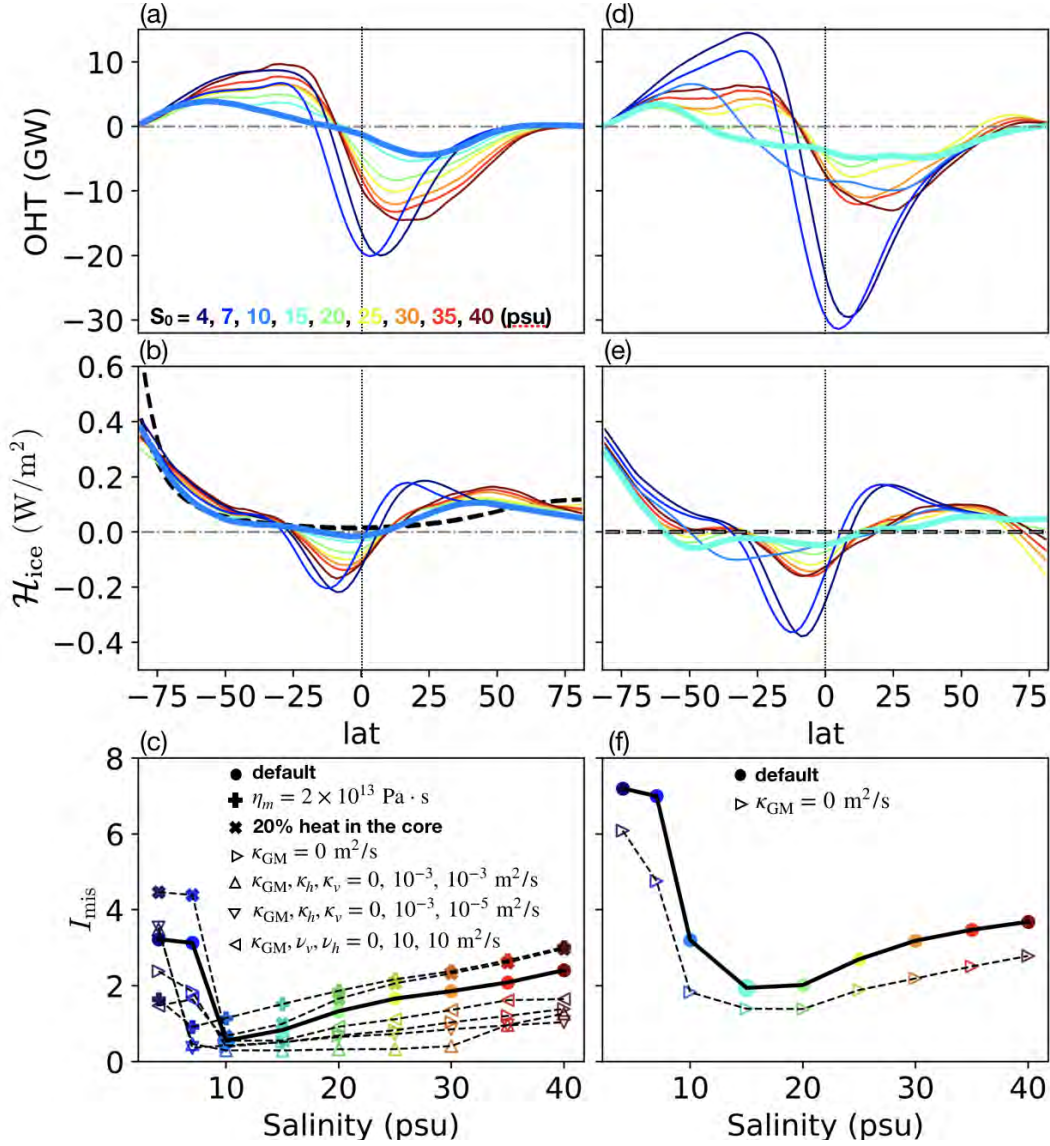
Fig. 4. Meridional heat transport and heat budget for the shell-heating scenario (left) and the core-heating scenario (right). The top panels show the vertically-integrated meridional ocean heat transport for various assumed S_0. Positive values denote northward heat transport. The middle panels show the inferred tidal heating $\hat{\mathcal{H}}_{\rm ice}$. The two black dashed curves in panel (b) are the profiles of $\mathcal{H}_{\rm ice}$ predicted by a model of tidal heating in the ice shell with $p_\alpha = -2$ and $p_\alpha = -1$, respectively: a more negative p_α indicates a stronger rheology feedback and thus yields a slightly more polar-amplified $\mathcal{H}_{\rm ice}$ profile. The black dashed curves in panel (e) coincide with the zero line, because $\mathcal{H}_{\rm ice} = 0$ when all the heating is in the core. The bottom panels show the mismatch index $I_{\rm mix}$, defined in Eq. (2). The heat transport and inferred tidal heating profiles corresponding to the best-match experiments are highlighted by thicker curves in top and middle rows. Filled dots connected by a thick solid line corresponds to the default setup (GM diffusivity $\kappa_{\rm GM} = 0.1$ m^2/s, horizontal/vertical diffusivity $\kappa_h = \kappa_v = 0.005$ m^2/s, horizontal/vertical viscosity $\nu_h = \nu_v = 50$ m^2/s, 100% heat produced in the ice shell, and melting-point ice viscosity $\eta_m = 10^{14}$ Pa·s). Other symbols represent sensitivity tests as indicated by perturbations from the default in the legend. Cold to warm colors indicate increasing salinity from $S_0 = 4$ to 40 psu.

196 The dissipation rate within the ocean driven by libration/tidal motions is also under debate (43–45) leading to
197 a wide range of possible diapycnal diffusivities. Assuming a dissipation rate given by *Rekier et al. 2019* (45), we
198 find the explicit vertical diffusivity in Enceladus to be around 5×10^{-3} m^2/s (derivations can be found in the SM
199 section 1B), which is orders of magnitude greater than the molecular diffusivity. We apply this diffusivity to both
200 vertical and horizontal directions in our default setup. In addition to the mixing induced by libration/tidal motions,
201 baroclinic eddies will tend to flatten the isopycnals. Instead of resolving baroclinic eddies, we parameterize them using
202 the Gent-McWilliams scheme commonly employed in terrestrial ocean models (46). In SM section 1B, we estimate the
203 GM diffusivity using scaling laws and find it to be around 0.1 m^2/s. We note in passing that this diffusivity is orders
204 of magnitude smaller than assumed in *Lobo et al. 2021* (37). who used values more typical of Earth's ocean. To test
205 our solutions' sensitivity to mixing parameters, we carried out further sets of experiments for all salinity scenarios
206 using different Gent-McWilliams diffusivity κ_{GM}, horizontal/vertical explicit diffusivity κ_h, κ_v and horizontal/vertical
207 viscosity ν_h, ν_v. The I_{mis} for the sensitivity tests are plotted on Fig. 4c using triangular markers. Just as in the
208 control experiments (solid line with filled dots), I_{mis} first decreases then increases with the assumed ocean salinity,
209 and a minimum is achieved near 10 psu. Interested readers can find a more detailed discussion in SM section 2B.

4. Exploring mechanisms with a conceptual model

211 The numerical solutions presented above suggest that if Enceladus' ocean is of intermediate salinity, near the transition
212 between an α ocean and a β ocean, then equatorial convergence of heat is minimized, allowing a thick equatorial ice
213 shell to be maintained. This is much less likely in very fresh or very salty oceans. Here, we build a conceptual model
214 to highlight the physical processes that controls the circulation strength and explore a wider range of parameter space
215 that can be applied to other icy moons.

216 We represent the overall density contrast using the equator minus north pole density difference $\Delta\rho$. The temperature-
217 related density anomaly is $-\alpha_T \Delta T$, and salinity-related one is $\beta_S \Delta S$, where ΔT and ΔS are the potential temperature
218 and salinity anomaly at the equator relative to the north pole. We expect the mass transport by overturning circulation
219 Ψ to vary proportionally with $\Delta\rho$. For simplicity, we assume a linear form

$$\Psi = A(-\alpha_T \Delta T + \beta_S \Delta S), \tag{3}$$

221 where the constant A maps the density contrast on to the vigor of the overturning circulation, $\beta_S \approx 8 \times 10^{-4}$/psu for
222 all S_0, but α_T depends sensitively on S_0, as given by the Gibbs Seawater Toolbox (16).

223 The temperature contrast ΔT is determined by the pressure-induced freezing point shift from the north pole to
224 the equator[**],

$$\Delta T = b_0 \Delta P = b_0 \rho_i g \Delta H, \tag{4}$$

226 where $b_0 = -7.61 \times 10^{-4}$ K/dbar, $\rho_i = 917$ kg/m^3 is the ice density, $g = 0.113$ m/s^2 is the surface gravity of Enceladus
227 and $\Delta H = 11$ km is the difference in ice thickness between the equator and the north pole.

228 The lateral salinity flux is given by the product of Ψ and a salinity contrast ΔS and balances the salinity flux due
229 to freezing and melting yielding (see a detailed derivation in *Marshall & Radko 2003* (49)):

$$|\Psi| \Delta S = \rho_0 S_0 \Delta q \times (\pi a^2) \tag{5}$$

231 Here, Δq, the difference in the freezing rate between equator and pole, is chosen to be 4 km/Myr based on Fig.1b.
232 $a = 250$ km is the radius of Enceladus, and S_0 is the mean salinity. The fact that Ψ and ΔS appear as a product
233 indicates that the salinity gradient will weaken as the overturning circulation strengthens for fixed salinity forcing.

234 Combining Eq (3), Eq (4) and Eq (5), we can solve for ΔS and Ψ. The only tunable parameter here is A, which
235 controls the strength of the overturning circulation and can be adjusted to fit that obtained in our ocean model. With
236 A set to 4.5×10^{13} kg/s, we obtain the solutions shown by the open circles in Fig.2c (the size of the circle reflect the
237 amplitude of Ψ). The conceptual model solution broadly captures the behavior of the numerical simulations (filled
238 circles), including the strengthening of the overturning circulation and the weakening of salinity gradient away from
239 the transition zone separating the alpha ocean and beta ocean.

240 What is the all-important heat flux implied by our conceptual model? Analogously to Eq (5), the meridional heat
241 transport can be written

$$\mathcal{H}_{\mathrm{ocn}} = \frac{C_p \Psi \Delta T}{4\pi a^2}. \tag{6}$$

[**]Ocean temperature at the water-ice interface is relaxed tightly toward the local freezing point, which varies by around 0.1K across latitude. Reducing the meridional temperature contrast by only 10% (ocean temperature deviates $\delta T = 0.01$K from the freezing point) would induce a heat flux of $\gamma_T C_p \rho_0 \delta T = 400$ mW/m^2 ($\gamma_T = 10^{-5}$ m/s is the water-ice exchange coefficient for temperature, $C_p = 4000$ J/kg/K is the heat capacity of water and ρ_0 is the reference water density given by Eq.5 in the SM), which is unacceptably large.

This is shown as a function of salinity and equator-to-pole thickness variations in Fig.5a. Recall that the water-ice heat exchange must be smaller than the heat conduction rate of 50 mW/m² to maintain observed thickness variations of the Enceladus ice shell. The likely/unlikely parameter regime is shaded white/red (24, 30–33). We see that a salinity between roughly 10-22 psu (marked by two vertical blue dashed lines) is required to maintain ice thickness variations as large as are seen on Enceladus.

5. Concluding Remarks

In conclusion, from knowledge of the geometry of the ice shell on Enceladus we have deduced likely patterns of (i) salinity gradients associated with freezing and melting and (ii) under-ice temperature gradients due to the depression of the freezing point of water due to pressure. We have considered the resulting ocean circulation driven by these boundary conditions, along with the effect of putative heat fluxes emanating from the bottom if tidal dissipation in the core is significant. We find that the ocean circulation strongly depends on its assumed salinity. If the ocean is fresh, sinking occurs at the poles driven by the meridional temperature gradient; if the ocean is salty, sinking occurs at the equator driven by the salinity gradient. In both limits (very salty and very fresh), heat is converged equatorward by the overturning circulation at rates which imply melting of the ice sheet (33). This is because the freezing point of water at the poles is higher than that at the equator and the magnitude of heat convergence is so large that it cannot be lost to space by heat conduction though the thick equatorial ice. As a result, ice geometry will be flattened.

When salinity is in an intermediate range (our calculations suggest the most plausible range is 10-20 psu) and heat production occurs primarily in the ice shell, the temperature and salinity-driven overturning circulation largely cancel one-another and the equatorward heat transport is small enough that a plausible heat balance can be achieved in the ice shell. Such cancellation is only possible at salinities lower than 22 psu. This salinity represents the transition between the alpha ocean, with polar sinking and equatorial upwelling (Fig.3 first column), from the beta ocean, featuring the opposite (Fig.3 third column). As discussed in the introduction, such lower salinities are consistent with the predictions from chemical equilibrium models of the interaction between the rocky core and the ocean (18–20). The circulation and heat transport remain qualitatively similar when changing the partition of heat generation between the ice shell and the silicate core. However, because the ice heat production is assumed to be low in the core-heating scenario, the equatorward heat convergence cannot be balanced, making this scenario less relevant.

Insights from this study may also have implications for other icy moons. For example, Europa may have a salinity as high as 50 psu, as implied by the strong magnetic induction field measured by the Galileo mission (50) – see *Zolotov & Shock 2001* (51), *Khurana et al. 2009* (52), *Vance et al. 2020* (53) for discussion of possible ocean compositions together with uncertainties. At salinities as high as 50 psu, the ice pump mechanism and associated dynamics (as discussed above) would remove any fluctuations in the ice shell thickness, leaving a relatively flat ice sheet. Applying our simplified model to Europa in Fig.5b, the predicted water-ice heat exchange becomes unphysically large (marked by the thick contour) when the equator-to-pole thickness variation is beyond 20% (indicated by the two horizontal blue dashed lines). This is consistent with the observation that the mean ice thickness is less than 15 km (best match at 4 km) (50, 54) and that no fissures that mimic the "tiger stripes" of Enceladus have been found on Europa. For icy moons with thicker ice shells, such as Dione, Titan, Ganymede and Callisto, the high pressure under the ice shell would remove the anomalous expansion for all salinities, making it impossible for the alpha and beta effects to cancel one another. Furthermore, the ice flow becomes very efficient, because it is proportional to the ice thickness cubed (see Eq.11 in SM). Our conceptual model indeed indicates that icy ocean worlds with thick ice shells are likely to have small spatial shell thickness variations. This is consistent with shell thickness reconstructions based on gravity and shape measurements (55–58). With future space missions (e.g., Europa Clipper), we expect that improved observations of gravity, topography, and induced magnetic fields for icy moons will provide stronger constraints on ocean salinity and ice shell structure.

1. F Postberg, et al., Sodium salts in e-ring ice grains from an ocean below the surface of enceladus. *Nature* **459**, 1098–1101 (2009).
2. P Thomas, et al., Enceladus's measured physical libration requires a global subsurface ocean. *Icarus* **264**, 37–47 (2016).
3. G Choblet, et al., Powering prolonged hydrothermal activity inside Enceladus. *Nat. Astron.* **1**, 841–847 (2017).
4. M Beuthe, Enceladus's crust as a non-uniform thin shell: Ii tidal dissipation. *Icarus* **332**, 66 – 91 (2019).
5. JH Waite, et al., Cassini Ion and Neutral Mass Spectrometer: Enceladus Plume Composition and Structure. *Science* **311**, 1419–1422 (2006).
6. HW Hsu, et al., Ongoing hydrothermal activities within enceladus. *Nature* **519**, 207–210 (2015).
7. JH Waite, et al., Cassini finds molecular hydrogen in the Enceladus plume: Evidence for hydrothermal processes. *Science* **356**, 155–159 (2017).
8. F Postberg, et al., Macromolecular organic compounds from the depths of enceladus. *Nature* **558**, 564–568 (2018).
9. RS Taubner, et al., Biological methane production under putative enceladus-like conditions. *Nat. communications* **9**, 1–11 (2018).

Kang *et al.*

Water-ice heat exchange (mW/m²)

(a) Enceladus   (b) Europa
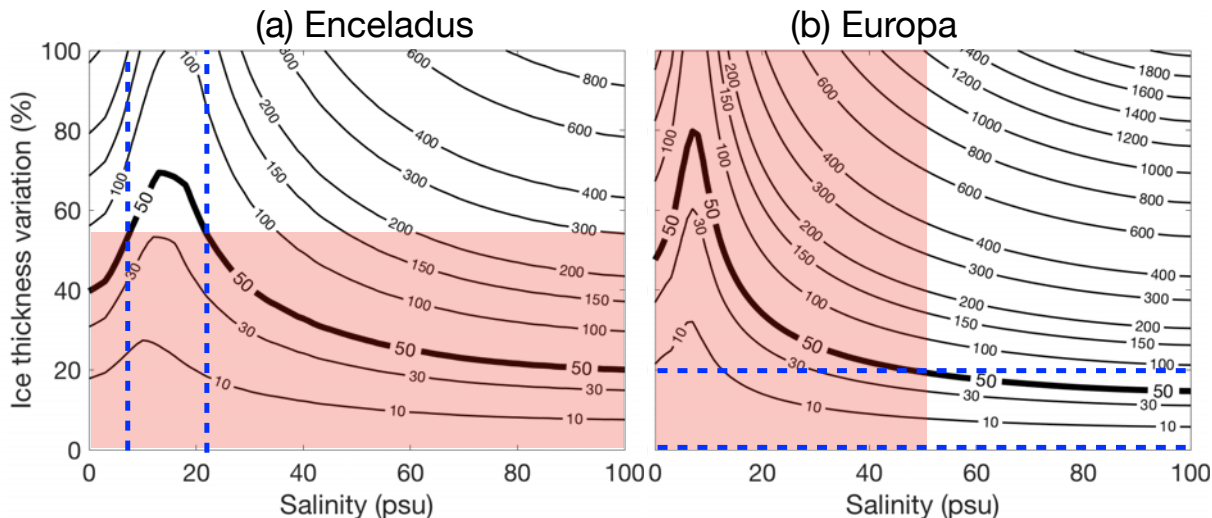
Fig. 5. The water-ice heat exchange in equatorial regions for Enceladus (left) and Europa (right) predicted by our conceptual model (Eq.6) as a function of salinity and equator-to-pole percentage ice thickness variation (equatorial minus polar ice thickness divided by the mean). A degree-2 poleward-thinning structure is assumed and physical parameters are defined in the SM Table S1. Parameter regimes that are not consistent with observations are shaded in red: the ice shell of Enceladus is thought to have large thickness variations (24, 30–33) and the salinity of Europa is thought to exceed 50 psu (50). The 50 mW/m² contour is highlighted by a thicker curve; heat exchange rates that exceed this are considered unphysical as the equatorial ice sheet of both Enceladus and Europa only allow ∼40 mW/m² or so of heat flux to conduct through. The equatorial heat loss rates are similar on the two icy moons because the likely thin ice shell on Europa (15km) compensates for its relatively high surface temperature (110K). Our simplified model suggests that salinities on Enceladus and ice thickness variations for Europa lie in the region enclosed by the blue dashed lines. The most plausible ice-thickness variations and salinity on Enceladus and Europa thus lie in the white areas between the blue dashed lines.

299   10. CR Glein, JH Waite, The Carbonate Geochemistry of Enceladus' Ocean. *Geophys. Res. Lett.* **47**, 591 (2020).
300   11. CJ Hansen, et al., Enceladus' Water Vapor Plume. *Science* **311**, 1422–1425 (2006).
301   12. CJA Howett, JR Spencer, J Pearl, M Segura, High heat flow from Enceladus's south polar region measured using 10-600 cm-1 Cassini/CIRS data. *J. Geophys. Res.* **116**, 189 (2011).
302   13. JR Spencer, et al., Enceladus Heat Flow from High Spatial Resolution Thermal Emission Observations. *Eur. Planet. Sci. Congr.* **8**, EPSC2013–840 (2013).
303   14. C McCarthy, RF Cooper, Tidal dissipation in creeping ice and the thermal evolution of Europa. *Earth Planet. Sci. Lett.* **443**, 185–194 (2016).
304   15. G Tobie, A Mocquet, C Sotin, Tidal dissipation within large icy satellites: Applications to europa and titan. *Icarus* **177**, 534–549 (2005).
305   16. TJ McDougall, PM Barker, Getting started with teos-10 and the gibbs seawater (gsw) oceanographic toolbox. *SCOR/IAPSO WG* **127**, 1–28 (2011).
306   17. J Cullum, DP Stevens, MM Joshi, Importance of ocean salinity for climate and habitability. *Proc. Natl. Acad. Sci.* **113**, 4278–4283 (2016).
307   18. MY Zolotov, An oceanic composition on early and today's Enceladus. *Geophys. Res. Lett.* **34** (2007).
308   19. MY Zolotov, F Postberg, Can nano-phase silica originate from chondritic fluids? the application to enceladus' sio2 particles. *LPI*, 2496 (2014).
309   20. C Glein, F Postberg, S Vance, The geochemistry of enceladus: Composition and controls. *Enceladus icy moons Saturn* **39** (2018).
310   21. AP Ingersoll, M Nakajima, Controlled boiling on enceladus. 2. model of the liquid-filled cracks. *Icarus* **272**, 319–326 (2016).
311   22. MG Fox-Powell, CR Cousins, Partitioning of crystalline and amorphous phases during freezing of simulated enceladus ocean fluids. *J. Geophys. Res. Planets* **126**, e2020JE006628 (2021).
312   23. BJ Travis, G Schubert, Keeping Enceladus warm. *Icarus* **250**, 32–42 (2015).
313   24. DJ Hemingway, T Mittal, Enceladus's ice shell structure as a window on internal heat production. *Icarus* **332**, 111–131 (2019).
314   25. O Soucek, et al., Tidal dissipation in Enceladus' uneven, fractured ice shell. *Icarus* **328**, 218–231 (2019).
315   26. G Robuchon, et al., Coupling of thermal evolution and despinning of early iapetus. *Icarus* **207**, 959–971 (2010).
316   27. D Shoji, H Hussmann, K Kurita, F Sohl, Ice rheology and tidal heating of enceladus. *Icarus* **226**, 10–19 (2013).
317   28. M Běhounková, G Tobie, G Choblet, O Čadek, Impact of tidal heating on the onset of convection in enceladus's ice shell. *Icarus* **226**, 898–904 (2013).
318   29. Y Gevorgyan, G Boué, C Ragazzo, LS Ruiz, AC Correia, Andrade rheology in time-domain. application to enceladus' dissipation of energy due to forced libration. *Icarus* **343**, 113610 (2020).
319   30. L Iess, et al., The Gravity Field and Interior Structure of Enceladus. *Science* **344**, 78–80 (2014).
320   31. M Beuthe, A Rivoldini, A Trinh, Enceladus's and Dione's floating ice shells supported by minimum stress isostasy. *Geophys. Res. Lett.* **43**, 10,088–10,096 (2016).
321   32. R Tajeddine, et al., True polar wander of Enceladus from topographic data. *Icarus* **295**, 46–60 (2017).
322   33. O Čadek, et al., Long-term stability of enceladus' uneven ice shell. *Icarus* **319**, 476–484 (2019).
323   34. G Tobie, G Choblet, C Sotin, Tidally heated convection: Constraints on Europa's ice shell thickness. *J. Geophys. Res - Atmospheres* **108**, 219 (2003).
324   35. AC Barr, AP Showman, Heat transfer in europa's icy shell in *Europa.* (Univ. Arizona Press), pp. 405–430 (2009).
325   36. Y Ashkenazy, R Sayag, E Tziperman, Dynamics of the global meridional ice flow of Europa's icy shell. *Nat. Astron.* **2**, 43–49 (2018).
326   37. AH Lobo, AF Thompson, SD Vance, S Tharimena, A pole-to-equator overturning circulation on enceladus. *Nat. Geosci.*, 1–5 (2021).
327   38. E Lewis, R Perkin, Ice pumps and their rates. *J. Geophys. Res* **91**, 756–11 (1986).
328   39. A Czaja, J Marshall, The partitioning of poleward heat transport between the atmosphere and ocean. *J. atmospheric sciences* **63**, 1498–1511 (2006).
329   40. W Kang, G Flierl, Spontaneous formation of geysers at only one pole on enceladus's ice shell. *PNAS* **117**, 14764–14768 (2020).
330   41. Y Zeng, MF Jansen, Ocean circulation on enceladus with a high versus low salinity ocean. *arXiv preprint arXiv:2101.10530* (2021).
331   42. H Jeffreys, On fluid motions produced by differences of temperature and humidity. *Q. J. Royal Meteorol. Soc.* **51**, 347–356 (1925).
332   43. EMA Chen, F Nimmo, GA Glatzmaier, Tidal heating in icy satellite oceans. *Icarus* **229**, 11–30 (2014).
333   44. HCFC Hay, I Matsuyama, Nonlinear tidal dissipation in the subsurface oceans of Enceladus and other icy satellites. *Icarus* **319**, 68–85 (2019).
334   45. J Rekier, A Trinh, S Triana, V Dehant, Internal energy dissipation in enceladus's subsurface ocean from tides and libration and the role of inertial waves. *J. Geophys. Res. Planets* **124**, 2198–2212
335   (2019).
336   46. PR Gent, JC Mcwilliams, Isopycnal mixing in ocean circulation models. *J. Phys. Oceanogr.* **20**, 150–155 (1990).
337   47. KM Soderlund, Ocean Dynamics of Outer Solar System Satellites. *Geophys. Res. Lett.* **46**, 8700–8710 (2019).
338   48. JP Renaud, WG Henning, Increased Tidal Dissipation Using Advanced Rheological Models: Implications for Io and Tidally Active Exoplanets. *Astrophys. J.* **857**, 98 (2018).

49. J Marshall, T Radko, Residual-mean solutions for the antarctic circumpolar current and its associated overturning circulation. *J. Phys. Ocean.* **33**, 2341–2354 (2003).

50. K Hand, C Chyba, Empirical constraints on the salinity of the europan ocean and implications for a thin ice shell. *Icarus* **189**, 424–438 (2007).

51. MY Zolotov, EL Shock, Composition and stability of salts on the surface of europa and their oceanic origin. *J. Geophys. Res. Planets* **106**, 32815–32827 (2001).

52. KK Khurana, MG Kivelson, KP Hand, CT Russell, Electromagnetic induction from europa's ocean and the deep interior. *Robert. T. Pappalardo, William. B. McKinnon, K. Khurana, Ed. Eur. Univ. Ariz. Press. Tucson*, 572–586 (2009).

53. SD Vance, et al., Magnetic induction in convecting galilean oceans. *arXiv preprint arXiv:2002.01636* (2020).

54. RS Park, et al., Improved detection of tides at Europa with radiometric and optical tracking during flybys. *Planet. Space Sci.* **112**, 10–14 (2015).

55. M Zannoni, D Hemingway, LG Casajus, P Tortora, The gravity field and interior structure of dione. *Icarus*, 113713 (2020).

56. D Durante, D Hemingway, P Racioppa, L Iess, D Stevenson, Titan's gravity field and interior structure after cassini. *Icarus* **326**, 123–132 (2019).

57. F Nimmo, B Bills, Shell thickness variations and the long-wavelength topography of titan. *Icarus* **208**, 896–904 (2010).

58. SD Vance, et al., Magnetic induction in convecting galilean oceans. *arXiv preprint arXiv:2002.01636* (2020).

1

Supplementary Information for

How does salinity shape ocean circulation and ice geometry on Enceladus and other icy satellites?

Wanying Kang, Tushar Mittal, Suyash Bire, Jean-Michel Campin, and John Marshall

Wanying Kang

E-mail: wanying@mit.edu

This PDF file includes:

Supporting Information Text

1. Model description

A. An overview of the General Circulation Model. Our simulations are carried out using the Massachusetts Institute of Technology OGCM (MITgcm (1, 2)) configured for application to icy moons. Our purpose is to 1) simulate the large-scale circulation and tracer transport driven by under-ice salinity gradients induced by patterns of freezing and melting, under-ice temperature gradients due to the pressure-dependence of the freezing point of water and bottom heat fluxes associated with tidal dissipation in the core, 2) diagnose the water-ice heat exchange rate and, 3) examine whether this heat exchange is consistent with the heat budget of the ice sheet, comprising heat loss due to conduction, tidal heating in the ice sheet, and heating due to latent heat release on freezing, as presented graphically in Fig. 1 of the main text.

In our calculations the ice shell freezing/melting rate is derived from a model of ice flow (described below), based on observational inferences of ice shell thickness, prescribed and held constant: it is not allowed to respond to the heat/salinity exchange with the ocean underneath. To enable us to integrate our ocean model out to equilibrium on a 10,000 year timescales and to explore a wide range of parameters, we employ a zonally-symmetric configuration at relatively coarse resolution, and parameterize the diapycnal mixing, convection and baroclinic instability of small-scale turbulent processes that cannot be resolved. Each experiment is initialized from rest and a constant salinity distribution. The initial potential temperature at each latitude is set to be equal to the freezing point at the water-ice interface. The simulations are then launched for 10,000 years. By the end of 10,000 years of integration thermal equilibrium has been reached.

The model integrates the non-hydrostatic primitive equations for an incompressible fluid in height coordinates, including a full treatment of the Coriolis force in a deep fluid, as described in (1, 2). Such terms are typically neglected when simulating Earth's ocean because the ratio between the fluid depth and horizontal scale is small. Instead Enceladus' aspect ratio is order 40km/252km$\sim$ 0.16 and so not negligibly small. The size of each grid cell shrinks with depth due to spherical geometry and is accounted for by switching on the "deepAtmosphere" option of MITgcm. Since the depth of Enceladus' ocean is comparable to its radius, the variation of gravity with depth is significant. The vertical profile of gravity in the ocean and ice shell is given by, assuming a bulk density of $\rho_{\text{out}} = 1000$ kg/m^3:

$$g(z) = \frac{G\left[M - (4\pi/3)\rho_{\text{out}}(a^3 - (a-z)^3)\right]}{(a-z)^2}. \tag{1}$$

In the above equation, $G = 6.67 \times 10^{-11}$ N/m^2/kg^2 is the gravitational constant and $M = 1.08 \times 10^{20}$ kg and $a = 252$ km are the mass and radius of Enceladus.

Since it takes several tens of thousands of years for our solutions to reach equilibrium, we employ a moderate resolution of 2 degree (8.7 km) and run the model in a 2D, zonal-average configuration whilst retaining full treatment of Coriolis terms. By doing so, the zonal variations are omitted (the effects of 3D dynamics are to be explored in future studies). In the vertical direction, the 60 km ocean-ice layer is separated into 30 layers, each of which is 2 km deep. The ocean is encased by an ice shell with meridionally-varying thickness using MITgcm's "shelfice" and ice "boundary layer" module (3). We set the ice thickness H using the zonal average of the thickness map given by *Hemingway & Mittal 2019* (4), as shown by a solid curve in Fig.1b in the main text, and assume hydrostacy (i.e., ice is floating freely on the water). We employ partial cells to better represent the ice topography: water is allowed to occupy a fraction of the height of a whole cell with an increment of 10%.

B. Parameterization of subgridscale processes. Key processes that are not explicitly resolved in our model are diapycnal mixing, convection and baroclinic instability. Here we review the parameterizations and mixing schemes used in our model to parameterize them. Sensitivity tests of our solutions when mixing parameters are varied about reference values are presented in Section 2B.

Vertical mixing of tracers and momentum

To account for the mixing of momentum, heat and salinity by unresolved turbulence, in our reference calculation we set the explicit viscosity/diffusivity to 0.005 m^2/s. This is roughly 3 orders of magnitude greater than molecular diffusivity, but broadly consistent with dissipation rates suggested by *Rekier et al. 2019* for Enceladus (5), where both libration and tidal forcing are taken into account. According to (5), the tidal dissipation in the ocean is mostly induced by libration implying a global dissipation rate E of order 1 MW. Following *Wunsch & Ferrari 2004* (6), this suggests a vertical diffusivity given by

$$\kappa_v = \frac{\Gamma\varepsilon}{\rho_0 N^2}, \tag{2}$$

Wanying Kang, Tushar Mittal, Suyash Bire, Jean-Michel Campin, and John Marshall

where $\Gamma \sim 0.2$ is the efficiency at which dissipation of kinetic energy can be used to produce potential energy. $\varepsilon = E/V$ is the dissipation rate per area, and $V = 4\pi a^2 D$ is the total volume of the ocean. Here $\rho_0 \sim 1000$ kg/m^3 is the density of water. $N^2 = g(\partial \ln \rho / \partial z) \sim g(\Delta\rho/rho_0)/D$ is the Brunt-Vasala frequency of the ocean, where g and D are the gravity constant and ocean depth, respectively. $\Delta\rho/\rho_0$ can be estimated from $\alpha_T \Delta T_f$, where $\alpha_T \sim 5 \times 10^{-5}$/K is the thermal expansion coefficient and $\Delta T_f \sim 0.1$K is the difference between the freezing point underneath the equatorial and polar ice shell. Substituting into Eq.2, yields $\kappa_v \sim 0.005$ m^2/s, which is the default horizontal and vertical diffusivity used in our model. The diffusivity for temperature and salinity are set to be the same, so that the double diffusive effects are excluded.

The horizontal and vertical viscosity are set to 50 m^2/s to control grid-scale noise. To damp numerical noise induced by the stair-like ice topography, we also use a bi-harmonic hyperviscosity of 3×10^9 m^4/s and a bi-harmonic hyperdiffusivity of 5×10^7 m^4/s. Despite use of these viscous and smoothing terms, the dominant balance remains in the momentum equation is between the Coriolis force and the pressure gradient force and so zonal currents on the large-scale remain in thermal wind balance. To demonstrate that the viscous terms indeed play a minor role, Fig. S1 shows a typical example of the two-term balance in the thermal wind equation: $2\mathbf{\Omega} \cdot \nabla U = \partial b/a\partial\theta$. Since thermal wind balance is a consequence of geostrophic and hydrostatic balance and the latter is always a good approximation on the large scale, geostrophic balance is indeed well satisfied.
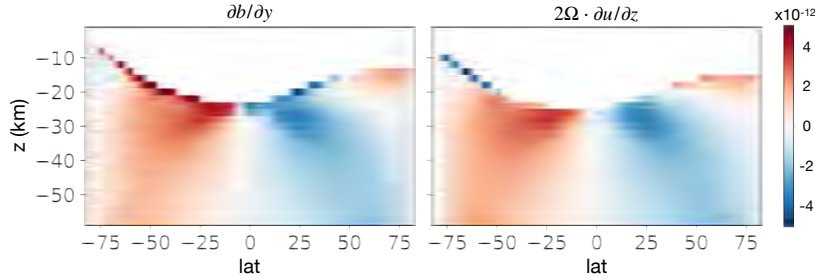
Fig. S1. Thermal wind balance in the control simulation. Panels shows the two terms in the thermal wind balance, $2\mathbf{\Omega} \cdot \nabla U$ and $\partial b/a\partial\phi$, respectively. Here Ω is the rotation rate of the moon, U is the zonal flow speed, $b = -g(\rho - \rho_0)/\rho_0$ is buoyancy, a is the moon's radius and ϕ is latitude.

Convection

Due to the coarse resolution of our model, convection cannot be resolved and must be parameterised. In regions that are convectively unstable, we set the diffusivity to a much larger value, 1 m^2/s, to represent the vertical mixing associated with convective overturns. Similar approaches are widely used to parameterize convection in coarse resolution ocean models (see, e.g. Klinger and Marshall, 1996) and belong to a family of convective adjustment schemes. Our results are not found to be sensitive to this choice provided the associated diffusive time scale $D^2/\nu_{\text{conv}} \approx 0.5$ yr is much shorter than the advective time scale $M_{\text{half}}/\Psi \approx 2000$ yrs (M_{half} is half of the total mass of the ocean and Ψ is the maximum meridional streamfunction in kg/s). It should be emphasized that away from boundary layers our solutions are close to geostrophic, hydrostatic and thermal wind balance and are not convectively unstable. However, convective heating from the bottom and/or salinization of water at the top can and do lead to convective instability which are mixed away diffusively.

Baroclinic instability

The large-scale currents set up in our model are in thermal wind balance with horizontal density gradients induced by under-ice temperature and salinity gradients. There is thus a store of available potential energy which will be tapped by baroclinic instability, a process which is not resolved in our model because of its zonally-symmetric configuration. Following an approach widely used in modeling Earth's ocean, we use the Gent-McWilliams (GM) scheme (7, 8) to parameterize the associated eddy-induced circulation and mixing of tracers along isopycnal surfaces. The key parameter that characterize the efficiency of the along-isopycnal mixing is the GM diffusivity κ_{GM}. According to *Visbeck et al. 1997* (9), κ_{GM} can be estimated by

$$\kappa_{\text{GM}} = \alpha l^2 \frac{f}{\sqrt{\text{Ri}}}, \qquad [3]$$

where $\frac{f}{\sqrt{\text{Ri}}}$ is proportional to the Eady growth rate, l is the width of the baroclinic zone, α=0.015 is a universal constant, f is the Coriolis parameter and Ri $= N^2/U_z$ is the Richardson number. We estimate l using the Rhine's scale $\sqrt{U/\beta}$, where U is the zonal flow speed and β is the meridional gradient of the Coriolis parameter. Substituting $N^2 \sim 10^{-11}$ s^{-2}, $f \sim 10^{-4}$ s^{-1}, $U \sim 10^{-3}$ m, and $\beta \sim 4 \times 10^{-10}$ s^{-1}m^{-1}, we get $\kappa_{\text{GM}} \sim 0.1$ m^2/s. It is notable that

this is 2-3 orders of magnitude smaller than the value used for Earth's ocean and those adopted by *Lobo et al. 2021* (10).

C. Equation of state and the freezing point of water. To make the dynamics as transparent as possible, we adopt a linear equation of state (EOS) to determine how density depends on temperature, salinity and pressure. The dependence of potential density ρ on potential temperature θ and salinity S is determined as follows:

$$\rho(\theta, S) = \rho_0 \left(1 - \alpha_T(\theta - \theta_0) + \beta_S(S - S_0)\right) \tag{4}$$

$$\rho_0 = \rho(\theta_0, S_0). \tag{5}$$

Here, ρ_0, θ_0 and S_0 are the reference potential density, potential temperature and salinity. α_T and β_S, the thermal expansion coefficient and the haline contraction coefficient, are set to the first derivative of density with respect to potential temperature and salinity at the reference point using the Gibbs Seawater Toolbox (11). We carried out two test experiments (one with $S_0 = 10$ psu and the other with $S_0 = 20$ psu) using the full "MDJWF" equation of state (12) and obtained almost identical results. To explore a wide range of background salinity, S_0 is prescribed to values between 4 psu and 40 psu. θ_0 is set to be the freezing temperature at S_0 and $P_0 = 2.2 \times 10^6$ Pa (this is the pressure under a 20.8 km thick ice sheet on Enceladus).

The freezing point of water T_f is assumed to depend on local pressure P and salinity S as follows,

$$T_f(S, P) = c_0 + b_0 P + a_0 S, \tag{6}$$

where $a_0 = -0.0575$ K/psu, $b_0 = -7.61 \times 10^{-4}$ K/dbar and $c_0 = 0.0901$ degC. The pressure P can be calculated using hydrostatic balance $P = \rho_i g H$ ($\rho_i = 917$ kg/m^3 is the density of the ice and H is the ice thickness).

D. Boundary conditions. Our ocean model is forced by heat and salinity fluxes from the ice shell at the top as well as heat fluxes coming from below.

Diffusion of heat through the ice

Heat loss to space by heat conduction through the ice $\mathcal{H}_{\text{cond}}$ is represented using a 1D vertical heat conduction model,

$$\mathcal{H}_{\text{cond}} = \frac{\kappa_0}{H} \ln\left(\frac{T_f}{T_s}\right), \tag{7}$$

where H is the thickness of ice (solid curve in Fig.1b of the main text), the surface temperature is T_s and the ice temperature at the water-ice interface is the local freezing point T_f (Eq. 6). We approximate the surface temperature T_s using radiative equilibrium based on the incoming solar radiation and obliquity ($\delta = 27°$) assuming an albedo of 0.81. The T_s profile is shown by the black solid curve in Fig.S2. Typical heat losses averaged over the globe are $\mathcal{H}_{\text{cond}} = 50$ mW/m^2.

Tidal heating in the core

Conductive heat loss is primarily balanced by tidal dissipation in the ice shell $\mathcal{H}_{\text{ice}}$ and the core $\mathcal{H}_{\text{core}}$ (dissipation in the ocean plays a negligible role) (5, 13–15). For each assumed heat partition between the shell and the core, we use the same meridional heating profiles for $\mathcal{H}_{\text{core}}$ and $\mathcal{H}_{\text{ice}}$ (see below). According to *Beuthe 2019*(16) and *Choblet et al. 2017*(17), the core dissipation $\mathcal{H}_{\text{core}}$ peaks at the two poles. We obtain the meridional heat profile using Eq.60 in *Beuthe 2019*(16) (Beuthe, personal communication),

$$\mathcal{H}_{\text{core}}(\phi) = \bar{\mathcal{H}}_{\text{core}} \cdot (1.08449 + 0.252257\cos(2\phi) + 0.00599489\cos(4\phi)), \tag{8}$$

where ϕ denotes latitude and $\bar{\mathcal{H}}_{\text{core}}$ is the global mean heat flux from the bottom. Since the global surface area shrinks going downward due to the spherical geometry, a factor of $(a - H)^2/(a - H - D)^2$ (H is ice thickness, D is ocean depth) needs to be considered when computing $\bar{\mathcal{H}}_{\text{core}}$. The expression within the bracket is normalized for the globe, adjusted to take account of the fact that our model only covers 84S-84N. Using the above formula, the bottom heat flux is twice as strong over the poles than equator.

Ice-ocean fluxes

At the upper (water-ice) boundary, freezing/melting induces a salinity/fresh water flux into the ocean (the ice salinity is assumed to be zero) and the ocean temperature at the upper boundary is relaxed to the local freezing point T_f set to the local salinity and pressure (Eq. 6).

$$\frac{dS_{\text{ocn-top}}}{dt} = \frac{qS_{\text{ocn-top}}}{\delta z} \tag{9}$$

$$\frac{dT_{\text{ocn-top}}}{dt} = \frac{1}{\delta z}(\gamma_T - q)(T_f - T_{\text{ocn-top}}) \tag{10}$$

Wanying Kang, Tushar Mittal, Suyash Bire, Jean-Michel Campin, and John Marshall
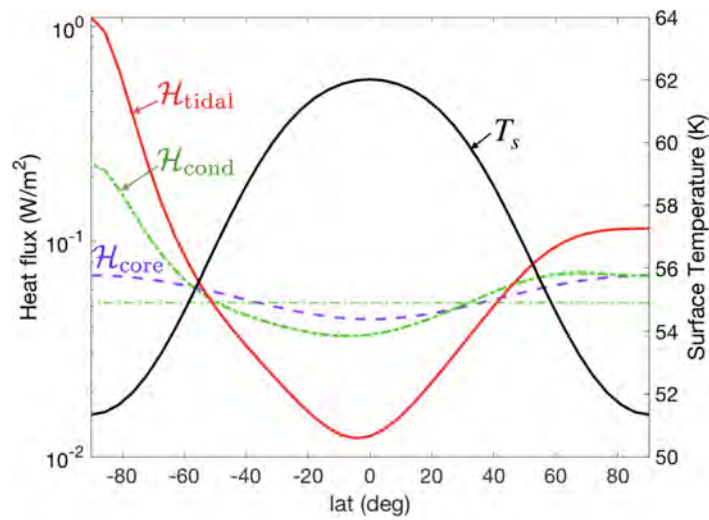
Fig. S2. Meridional profiles of heat fluxes and surface temperature. Heat fluxes are plotted using colored curves, with a scale on the left. Conductive heat loss $\mathcal{H}_{cond}$ (Eq. 7) is shown by a thick green dash-dotted line which, in the global average, is balanced by heat generation in the silicate core $\mathcal{H}_{core}$ (purple dashed line, Eq. 8) and $\mathcal{H}_{ice}$ (red solid line, Eq. 13). All heat fluxes are normalized to have the same global mean value of $\mathcal{H}_{cond}$. The surface temperature T_s (black solid line, axis on the right) is set to be in radiative equilibrium with the solar radiation and is warmer at the equator.

Here, $S_{\text{ocn-top}}$ and $T_{\text{ocn-top}}$ denote the upper boundary salinity and temperature, $\gamma_T = 10^{-5}$ m/s are the water-ice exchange coefficients for temperature and salinity, $\delta z = 2$ km is the vertical resolution of the model and q is the freezing rate in m/s (note that q is orders of magnitude smaller than γ_T). Note that q is prescribed rather than being dependent on the heat flux exchange across the water-ice boundary layer. Readers interested in the formulation of a freely evolving ice-water system are referred to the method section of *Kang et al. 2021* (18) and *Losch 2008* (3). Momentum is relaxed to zero at a rate of $\gamma_M = 10^{-3}$ m/s at the upper and lower boundaries.

Ice flow model

We prescribe q using the divergence of the ice flow, assuming the ice sheet geometry is in equilibrium. We use an upside-down land ice sheet model following *Ashkenazy et al. 2018* (19). The ice flows down its thickness gradient, driven by the pressure gradient induced by the spatial variation of the ice top surface, somewhat like a second order diffusive process. At the top, the speed of the ice flow is negligible because the upper part of the shell is so cold and hence rigid; at the bottom, the vertical shear of the ice flow speed vanishes, as required by the assumption of zero tangential stress there. This is the opposite to that assumed in the land ice sheet model. In rough outline, we calculate the ice flow using the expression below obtained through repeated vertical integration of the force balance equation (the primary balance is between the vertical flow shear and the pressure gradient force), using the aforementioned boundary conditions to arrive at the following formula for ice transport $\mathcal{Q}$,

$$
\begin{aligned}
\mathcal{Q}(\phi) &= \mathcal{Q}_0 H^3 (\partial_\phi H / a) \\
\mathcal{Q}_0 &= \frac{2(\rho_0 - \rho_i)g}{\eta_{\text{melt}}(\rho_0/\rho_i)\log^3(T_f/T_s)} \int_{T_s}^{T_f} \int_{T_s}^{T(z)} \exp\left[-\frac{E_a}{R_g T_f}\left(\frac{T_f}{T'} - 1\right)\right] \log(T') \, \frac{dT'}{T'} \, \frac{dT}{T}.
\end{aligned}
\tag{11}
$$

Here, ϕ denotes latitude, $a = 252$ km and $g = 0.113$ m/s^2 are the radius and surface gravity of Enceladus, T_s and T_f are the temperature at the ice surface and the water-ice interface (equal to local freezing point, Eq. 6), and $\rho_i = 917$ kg/m^3 and ρ_0 are the ice density and the reference water density (Eq. 4). $E_a = 59.4$ kJ/mol is the activation energy for diffusion creep, $R_g = 8.31$ J/K/mol is the gas constant and η_{melt} is the ice viscosity at the freezing point. The latter has considerable uncertainty (10^{13}-10^{16} Pa·s) (20) but we choose to set $\eta_{\text{melt}} = 10^{14}$ Pa·s.

In steady state, the freezing rate q must equal the divergence of the ice transport thus:

$$
q = -\frac{1}{a\cos\phi}\frac{\partial}{\partial\phi}(Q\cos\phi).
\tag{12}
$$

As shown by the dashed curve in Fig.1b of the main text, ice melts in high latitudes and forms in low latitudes at a rate of a few kilometers every million years. A more detailed description of the ice flow model can be found in *Kang and Flierl 2020* (21) and *Ashkenazy et al. 2018* (19). Freezing and melting leads to changes in local salinity and thereby a buoyancy flux. At $S_0 = 30$ psu, the salinity-associated buoyancy flux is approximately $gq\beta_S S_0 \approx 10^{-13}$ m^2/s^3, which is 3-6 orders of magnitude smaller than the buoyancy flux used by *Lobo et al. 2021* (10).

E. Model of tidal dissipation in the ice shell. Enceladus's ice shell is periodically deformed by tidal forcing and the resulting strains in the ice sheet produce heat. We follow *Beuthe 2019* (16) to calculate the implied dissipation rate. Instead of repeating the whole derivation here, we only briefly summarize the procedure and present the final result. Unless otherwise stated, parameters are the same as assumed in *Kang & Flierl 2020* (21).

Tidal dissipation consists of three components (16): a membrane mode $\mathcal{H}_{\text{ice}}^{\text{mem}}$ due to the extension/compression and tangential shearing of the ice membrane, a mixed mode $\mathcal{H}_{\text{ice}}^{mix}$ due to vertical shifting, and a bending mode $\mathcal{H}_{\text{ice}}^{bend}$ induced by the vertical variation of compression/stretching. Following *Beuthe 2019* (16), we first assume the ice sheet to be completely flat. By solving the force balance equation, we obtain the auxiliary stress function F, which represents the horizontal displacements, and the vertical displacement w. The dissipation rate $\mathcal{H}_{\text{ice}}^{\text{flat,x}}$ (where $x = \{\text{mem}, \text{mix}, \text{bend}\}$) can then be written as a quadratic form of F and w. In the calculation, the ice properties are derived assuming a globally-uniform surface temperature of 60K and a melting viscosity of 5×10^{13} Pa·s.

Ice thickness variations are accounted for by multiplying the membrane mode dissipation $\mathcal{H}_{\text{ice}}^{\text{flat,mem}}$, by a factor that depends on ice thickness. This makes sense because this is the only mode which is amplified in thin ice regions (see *Beuthe 2019* (16)). This results in the expression:

$$
\mathcal{H}_{\text{ice}} = (H/H_0)^{p_\alpha}\mathcal{H}_{\text{ice}}^{\text{flat,mem}} + \mathcal{H}_{\text{ice}}^{\text{flat,mix}} + \mathcal{H}_{\text{ice}}^{\text{flat,bend}},
\tag{13}
$$

where H is the prescribed thickness of the ice shell as a function of latitude and H_0 is the global mean of H. Since thin ice regions deform more easily and produce more heat, p_α is negative. Because more heat is produced in the ice shell, the overall ice temperature rises, which, in turn, further increases the mobility of the ice and leads to more heat production (the rheology feedback).

Wanying Kang, Tushar Mittal, Suyash Bire, Jean-Michel Campin, and John Marshall

Using reasonable parameters for Enceladus, $\mathcal{H}_{\text{ice}}$ turns out to be at least an order of magnitude smaller than the heat loss rate $\mathcal{H}_{\text{cond}}$. This is a universal flaw of present tidal dissipation models, and could be due to use of an over-simplified Maxwell rheology (22, 23). We therefore scale up $\mathcal{H}_{\text{ice}}$ by a constant factor to obtain the desired magnitude. The tidal heating profile corresponding to $p_\alpha = -1.5$ is the red solid curve plotted in Fig. S2. In Fig. 4(b,e) of the main text, we show the tidal heating profile for $p_\alpha = -1$ and $p_\alpha = -2$.

Symbol	Name	Definition/Value
	Enceladus parameters	
a	radius	252 km
δ	obliquity	27°
H	global mean ice thickness	20.8 km: ref (4)
D	global mean ocean depth	39.2 km: ref (4)
Ω	rotation rate	5.307×10^{-5} s^{-1}
g_0	surface gravity	0.113 m/s^2
$\bar{T}_s$	mean surface temperature	59K
	Europa parameters	
a	radius	1561 km
δ	obliquity	3.1°
H	global mean ice thickness	15 km: ref (24)
D	global mean ocean depth	85 km: ref (24)
Ω	rotation rate	2.05×10^{-5} s^{-1}
g_0	surface gravity	1.315 m/s^2
$\bar{T}_s$	mean surface temperature	110K
	Physical constants	
L_f	fusion energy of ice	334000 J/kg
C_p	heat capacity of water	4000 J/kg/K
$T_f(S,P)$	freezing point	Eq.6
ρ_i	density of ice	917 kg/m^3
ρ_w	density of the ocean	Eq.4
α, β	thermal expansion & saline contraction coeff.	using Gibbs Seawater Toolbox: ref (11)
κ_0	conductivity coeff. of ice	651 W/m: ref (25)
p_α	ice dissipation amplification factor	-2 ∼ -1
η_m	ice viscosity at freezing point	10^{14} Ps·s
	Default parameters in the ocean model	
$\nu_h,\ \nu_v$	horizontal/vertical viscosity	50 m^2/s
$\tilde{\nu}_h,\ \tilde{\nu}_v$	bi-harmonic hyperviscosity	3×10^9 m^4/s
$\kappa_h,\ \kappa_v$	horizontal/vertical diffusivity	0.005 m^2/s
κ_{GM}	Gent-McWilliams diffusivity	0.1 m^2/s
$(\gamma_T,\ \gamma_S,\ \gamma_M)$	water-ice exchange coeff. for T, S & momentum	$(10^{-5}, 10^{-5}, 10^{-3})$ m/s
g	gravity in the ocean	Eq.1
P_0	reference pressure	$\rho_i g_0 H = 2.16 \times 10^6$ Pa
T_0	reference temperature	$T_f(S_0, P_0)$
ρ_{w0}	reference density of ocean	Eq.5
$\mathcal{H}_{\text{cond}}$	conductive heat loss through ice	Eq.7, Fig.S2
$\mathcal{H}_{\text{ice}}$	tidal heating produced in the ice	Eq.13, Fig.S2
$\mathcal{H}_{\text{core}}$	bottom heat flux powered by the core	Eq.8, Fig.S2
A	surface albedo	0.81
T_s	surface temperature profile	Fig.S2

Table S1. Model parameters used in our study.

2. Exploring the sensitivity of ocean model solutions to parameters

A. Sensitivity to heat partition between the core and the shell. To examine the sensitivity of ocean circulation to core-shell heat partition, we repeat the same set of simulations with first 20% and then 100% heat produced in the core. The equilibrium ocean solutions are presented in Fig.S3 and Fig.S4 for the two heat partitions. Compared to our default calculation, the shell-heating scenario shown in Fig.3 of the main text, there is no qualitative change. This is to be expected because the dominant forcing of the flow is the salinity and heat exchange between ice and ocean: the vertical temperature gradient induced by bottom heating is much smaller than the temperature gradient at the water-ice interface induced by the pressure dependence of the freezing point of water. Bottom warming induces stronger stratification if the ocean is fresher than 22 psu (when $\alpha < 0$), and vice versa. As can be seen by comparing Fig.S3 and Fig.S4 with Fig.3, the strengthening/weakening of the stratification suppresses/enhances the vertical

extent over which the overturning circulation reaches into the deep ocean. The change is most pronounced at low salinity (4 psu), because the negative thermal expansion coefficient in a fresh ocean suppresses the parameterized convection, resulting in bottom water warming up. However, even with a mean salinity of 4 psu, the response of the dynamics to these stratification changes is rather small (compare the left columns of Fig.3 and Fig.S4 here). Note also that all experiments are run out to full equilibrium and so the bottom heat flux is transmitted upward to the water-ice interface without loss in an integral sense, but with ocean currents shaping regional contributions.
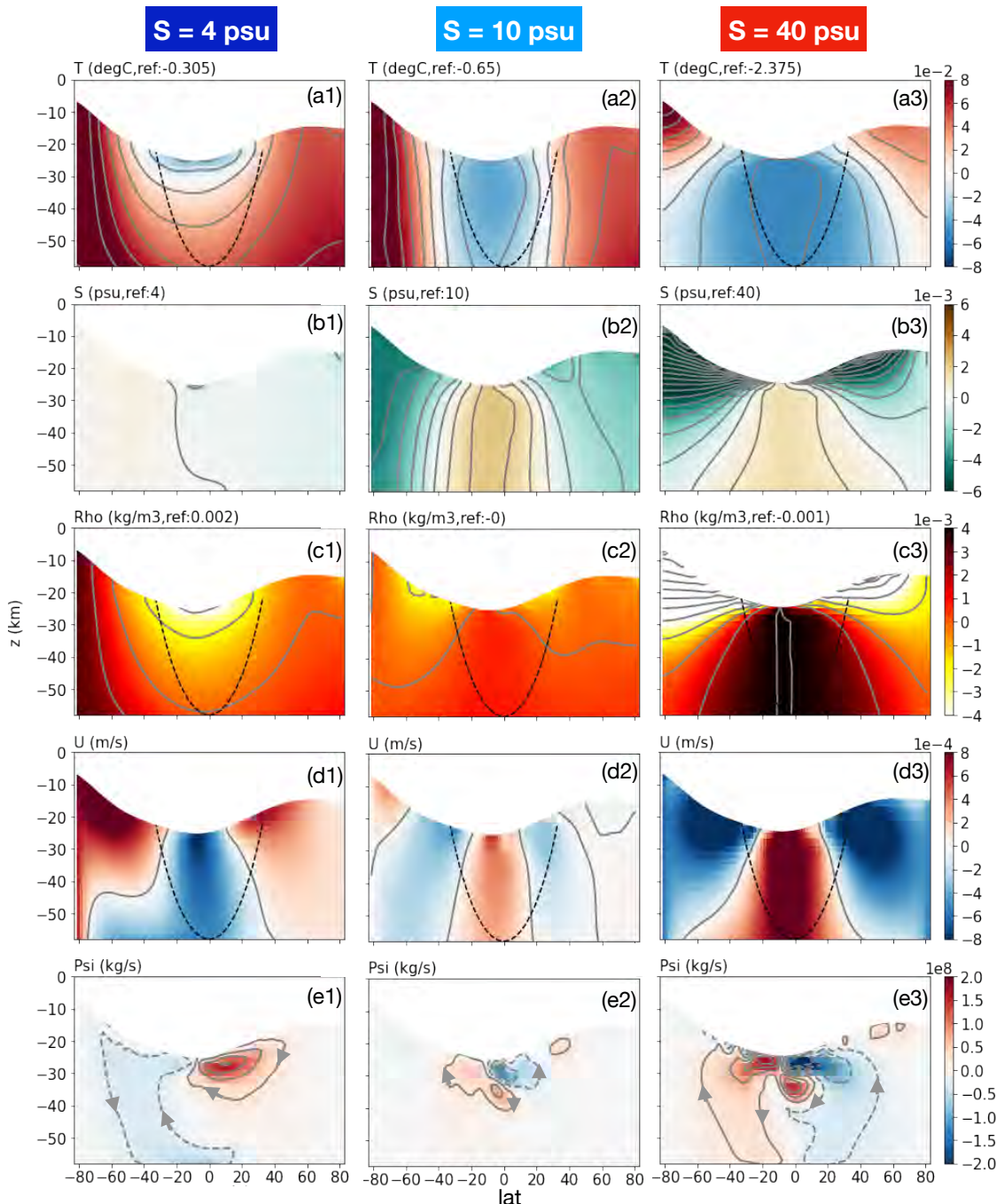
Fig. S3. As in Fig. 3 of the main text but with 20% heat assumed to be produced in the silicate core and 80% in the ice shell. Results are presented for three different salinities: 4 psu, 10 psu and 40 psu. Default mixing parameters are used.

B. Sensitivity to diffusivity and viscosity. To examine the sensitivity to diffusivity, we carried out three additional sets of experiments for the shell-heating scenario using different GM and diapycnal diffusivities: one with $\kappa_{\mathrm{GM}} = 0$ m^2/s, $\kappa_v = \kappa_h = 5 \times 10^{-3}$ m^2/s, one with $\kappa_{\mathrm{GM}} = 0$ m^2/s, $\kappa_v = \kappa_h = 10^{-3}$ m^2/s, and the third with $\kappa_{\mathrm{GM}} = 0$ m^2/s,

Wanying Kang, Tushar Mittal, Suyash Bire, Jean-Michel Campin, and John Marshall
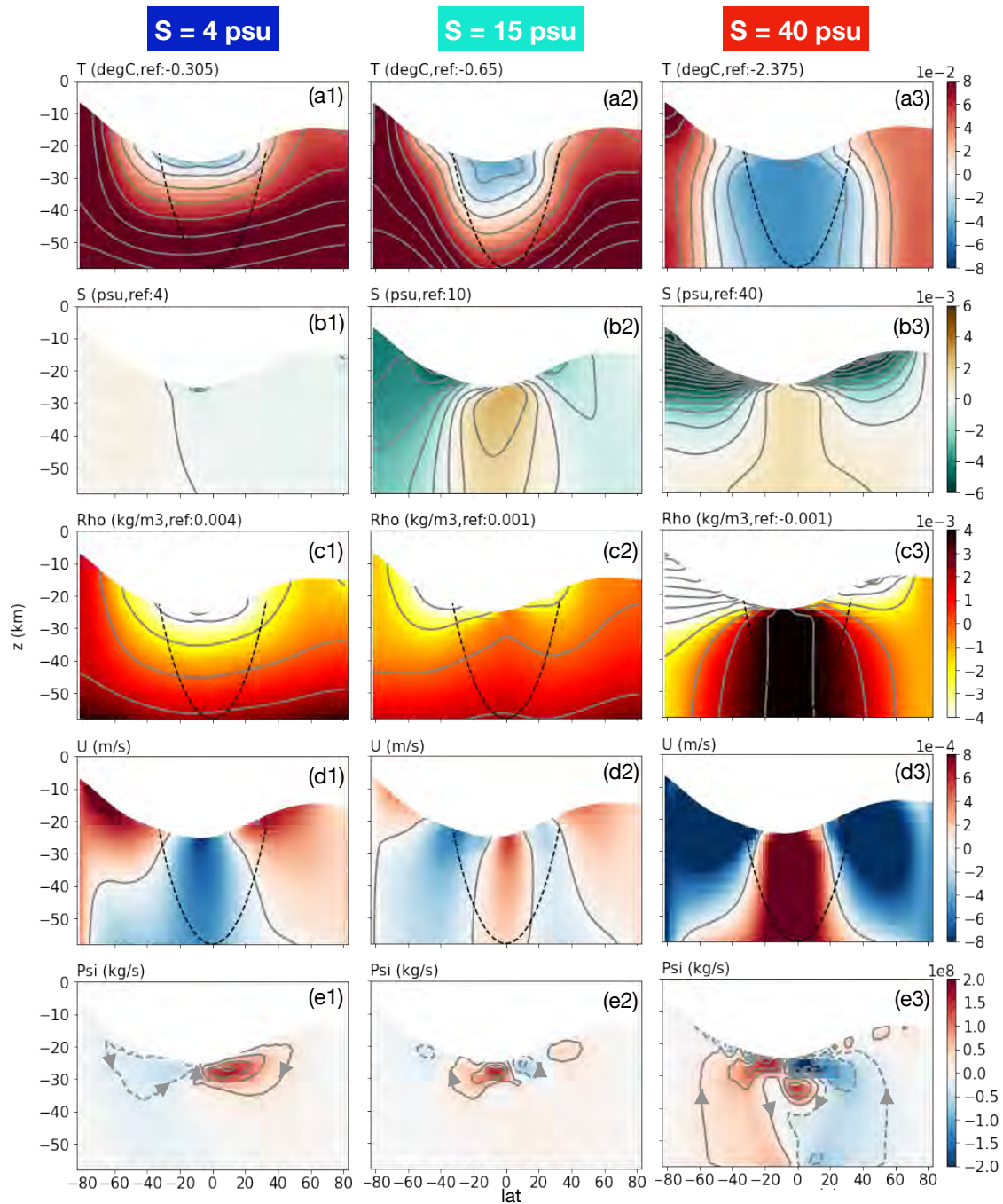
Fig. S4. As in Fig.S3 but with 100% heating in the core and none in the shell. Default mixing parameters are used.

$\kappa_v = 10^{-5}$ m^2/s, $\kappa_h = 10^{-3}$ m^2/s. The corresponding solutions for $S_0 = 4$, 10 and 40 psu are shown in Fig. S5, Fig. S6 and Fig. S7, respectively. The mismatch index that measures the discrepancy between the inferred and predicted ice tidal dissipation (Eq. 2 in the main text) are plotted on Fig. 4c in the main text using triangular markers.

On changing GM and diapycnal diffusivities, the meridional heat transport and hence the inferred tidal dissipation do not markedly change relative to the control experiments: compare the bottom panels of Fig. S5, Fig. S6 and Fig. S7 with Fig. 4b in the main text. The mismatch between the inferred tidal dissipation $\hat{\mathcal{H}}_{\mathrm{ice}}$ and the modeled dissipation $\mathcal{H}_{\mathrm{ice}}$ is smallest when the reference salinity is in the range 10-20 psu regardless of the spread of diffusivities being used. The ocean solutions also remain qualitatively similar to the control experiments shown in Fig. 3 in the main text. Low salinity cases have sinking over the poles, driven in the main by the density gradient associated with temperature anomalies (see left panels of Fig. S5, Fig. S6 and Fig. S7). The opposite is true for the high salinity cases (see the right panels). At intermediate salinities ($\sim$10 psu), the density gradient and overturning circulation are weak (see the middle panels), just as in the control solution (Fig. 3 in the main text). This weak circulation, in turn, leads to a weaker heat convergence toward the equator compared to the end-member cases (see Fig. S5f, Fig. S6f and Fig. S7f and Fig. 4b in the main text), and the resulting $\hat{\mathcal{H}}_{\mathrm{ice}}$ is more consistent with $\mathcal{H}_{\mathrm{ice}}$ (black dashed curves). This general trend is found in all diffusivity scenarios (Fig. 4c in the main text), suggesting that our main conclusions are indeed robust.

There are quantitative changes to our solutions, however. When GM is turned off, the overall stratification becomes weaker, the isopycnal slope becomes steeper (row-c of Fig. S5 and Fig. 3 in the main text), the salinity contrast is slightly reduced (row-b of Fig. S5 and Fig. 3 in the main text) and the circulation weakens. Furthermore, reducing the explicit diffusivity suppresses mixing and increases salinity/temperature variations over the globe (Fig. S6 and Fig. S7). These changes are particularly significant in the 40 psu case perhaps because the ocean circulation cannot be efficiently energized when the buoyancy source is located higher in the water column than the buoyancy sink (26).

We also carried out sensitivity tests for the core-heating scenario as shown in Fig. S8 for $S_0 = 4$, 10, 40 psu with $\kappa_{\mathrm{GM}} = 0$. Again, the solutions are very similar to those with a GM parameterization (Fig. S4), except for weaker stratification, weaker isopycnal slope, salinity contrast and circulation, relative to the shell-heating scenario with default parameters.

C. Sensitivity to assumed ice viscosity. The viscosity of the ice shell controls ice speeds (Eq. 11), and thereby the freezing/melting rate needed to maintain the observed ice geometry. However, due to our limited understanding of ice rheology, the uncertainties associated with the melting point ice viscosity η_m remain. To examine sensitivity we carried out an experiment with η_m set to 2×10^{13} Pa·s, 5 times lower than the default value. Solutions for $S_0 = 4$, 10, 40 psu are presented in Fig. S9. Decreasing the ice viscosity leads to a stronger salinity flux between the ocean and ice (Eq. 9) and stronger salinity variations. This can be clearly seen by comparing Fig. S9b with Fig. 3b of the main text. Since the overall salinity gradient increases, the density gradient also increases (Fig. S9c), and this in turn drives stronger circulation (Fig. S9e). In addition to these change, increasing ice mobility lowers the transitional salinity as shown by the Fig. 4c of the main text. That is because a more negative thermal expansion coefficient is required to cancel the salinity-induced density anomaly and achieve a minimum density gradient, indeed just as suggested by our conceptual model.

D. Experiments under hemispherically-symmetric forcing. In further tests we carried out experiments under hemispherically symmetric ice geometry and forcing allowing for comparison with theoretical model results reported by *Lobo et al. 2021* (10). A symmetric ice geometry is constructed by averaging the default ice thickness profile shown in Fig. 1b between the two hemispheres. The freezing/melting rate forcing is calculated as before (Eq 11) and the freezing point temperature imposed as a function of pressure. Symmetric ocean solutions are shown on the left column of Fig. S10 together with inferred tidal dissipation rates $\hat{\mathcal{H}}_{\mathrm{ice}}$ with default diffusivities ($\kappa_{\mathrm{GM}} = 0.1$ m^2/s, $\kappa_v = \kappa_h = 5 \times 10^{-3}$ m^2/s). The mean salinity is set to 30 psu to avoid anomalous expansion effects, and we assume all heat is produced in the ice shell. This broadly mimics the setup used by *Lobo et al. 2021* (10).

As found by *Lobo et al. 2021* (10), the near-surface isopycnals tilt downward in polar regions (Fig. S10-c1), driving meridional circulation confined to the near-surface layer (Fig. S10-e1). As in *Lobo et al. 2021* (10), we explored the sensitivity of our solution to mixing coefficients. The middle and right columns of Fig. S10 present solutions obtained using two different diapycnal diffusivities with $\kappa_{\mathrm{GM}} = 0$ m^2/s. By turning off the GM parameterization we again observe the circulation and stratification becoming weaker (Fig. S10-e2 and Fig. S10-c2). Furthermore, when lower diapycnal diffusivity is used, the stratification strengthens (Fig. S10-c3) and the circulation becomes weaker and shallower (Fig. S10-e3).

Finally, it should be noted that the GM diffusivity used here, $\kappa_{\mathrm{GM}} = 0.1$ m^2/s, is estimated based on our arguments that lateral mixing scales are a few kilometers and the eddy flow speed a few millimeters per second (see Eq 3). This
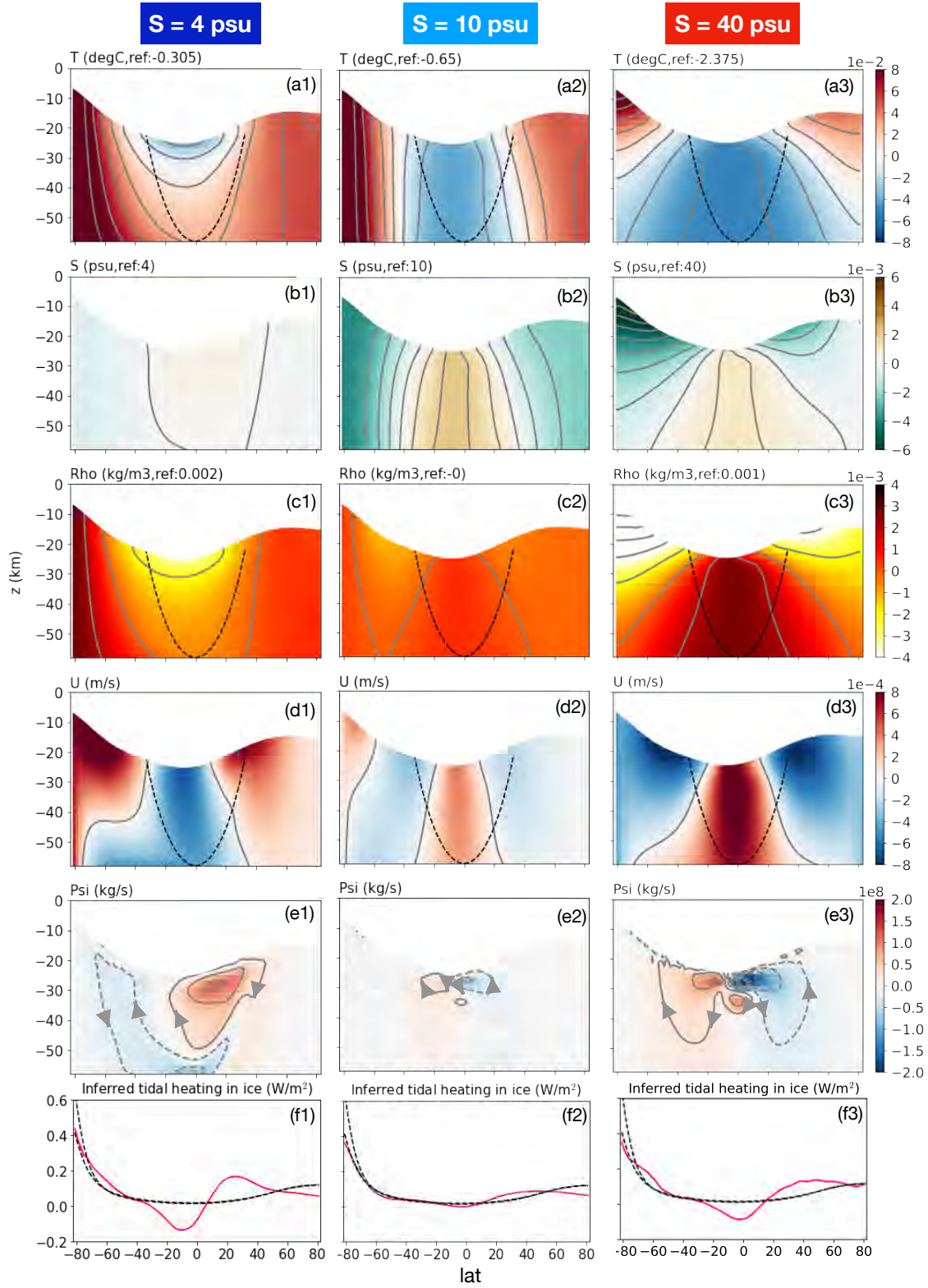
Fig. S5. The 100% shell-heating solution with default parameters except $\kappa_{\mathrm{GM}} = 0$ m^2/s. Row (a-e) are the same figure as in Fig.3 of the main text. Row (f) is similar to Fig. 4(b,e) of the main text and shows the inferred tidal dissipation $\hat{\mathcal{H}}_{\mathrm{ice}}$ (red solid line, calculated using Eq. 1 in the main text), compared with the dissipation rate predicted by our tidal dissipation model (black dashed lines, Eq.13).
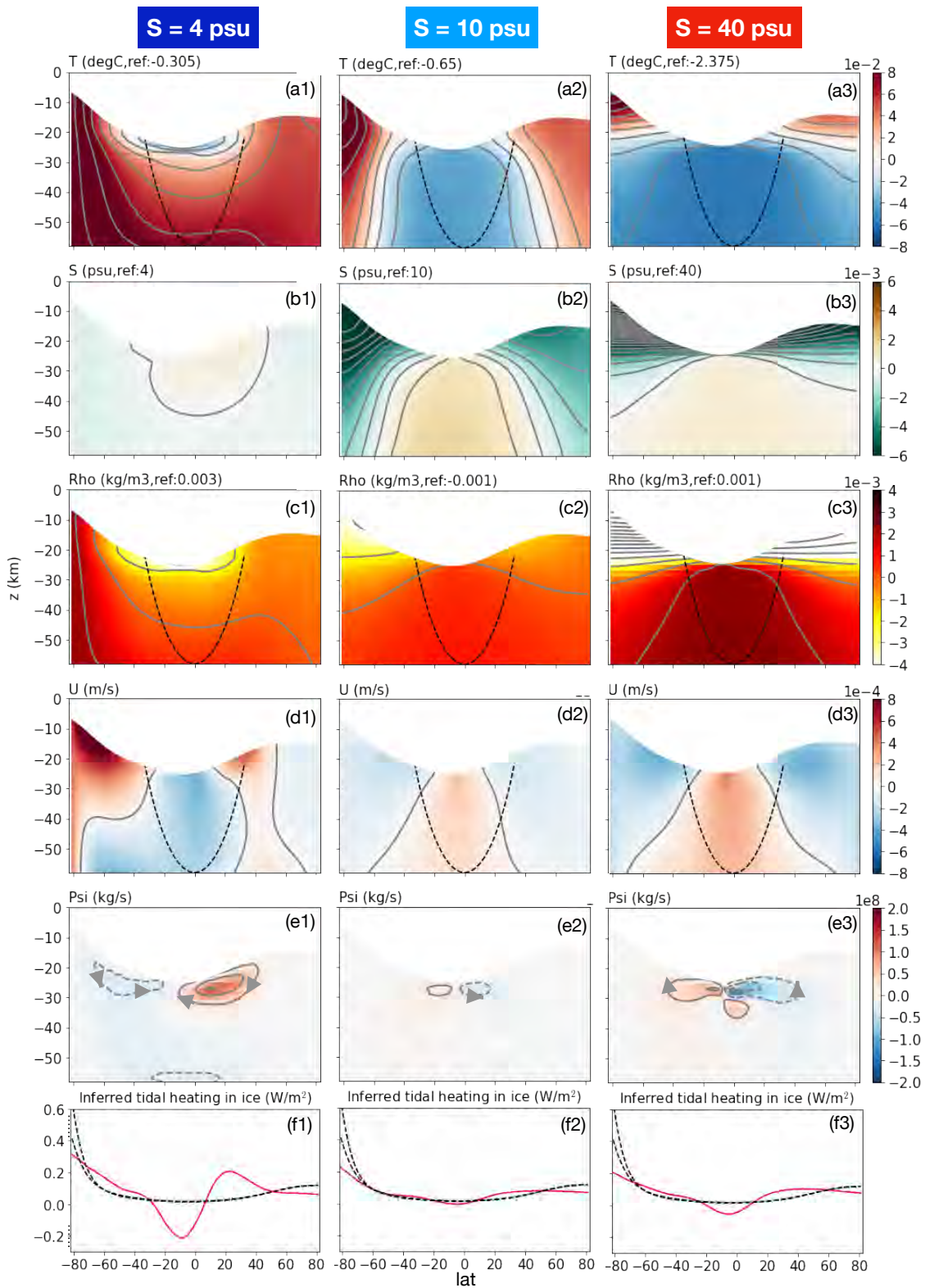
Fig. S6. The sensitivity of the 100% shell-heating solution to lower explicit diffusivity ($\kappa_{\mathrm{GM}} = 0$ m^2/s, $\kappa_v = \kappa_h = 10^{-3}$ m^2/s), set out as in Fig. S5.
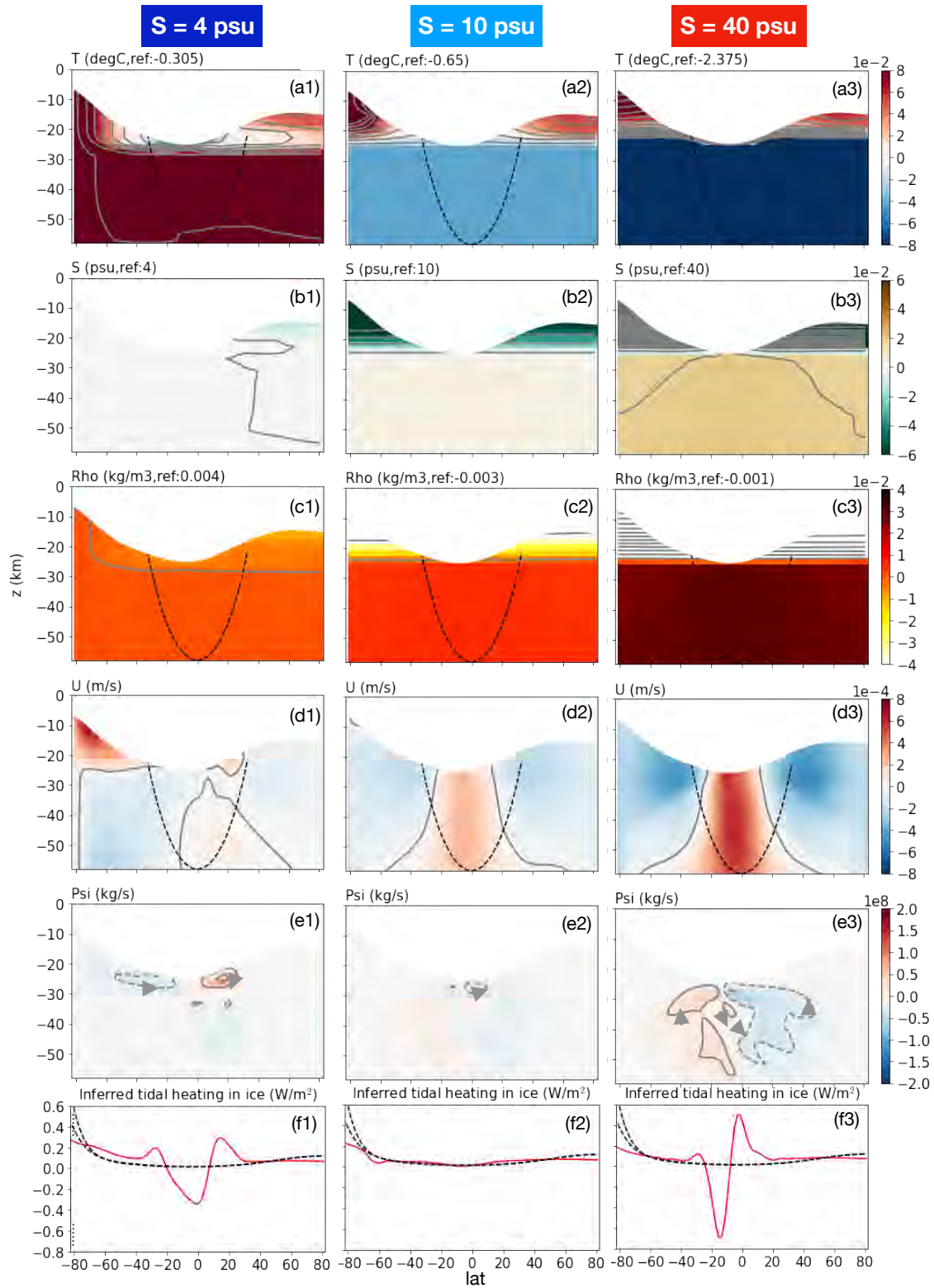
Fig. S7. The sensitivity of the 100% shell-heating solution to even lower explicit diffusivity ($\kappa_{\mathrm{GM}} = 0$ m^2/s, $\kappa_v = 10^{-5}$ m^2/s, $\kappa_h = 10^{-3}$ m^2/s), set out as in Fig. S5. The interval between salinity and density contours are 20 times larger than in other plots.
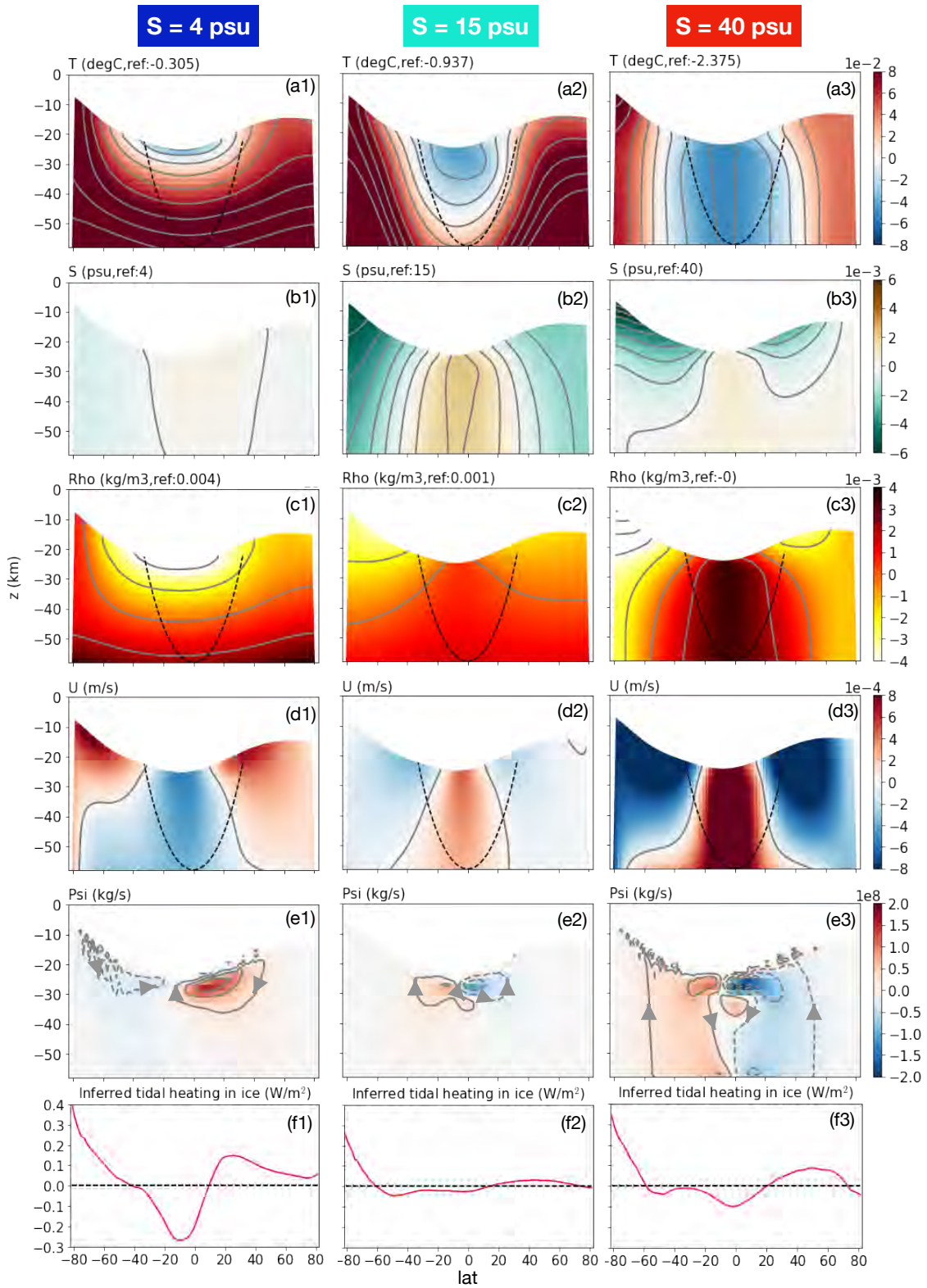
Fig. S8. The sensitivity of the 100% core-heating solution to zero GM diffusivity ($\kappa_{\mathrm{GM}} = 0$ m^2/s, $\kappa_v = 10^{-5}$ m^2/s, $\kappa_h = 10^{-3}$ m^2/s), set out as in Fig. S5.

Wanying Kang, Tushar Mittal, Suyash Bire, Jean-Michel Campin, and John Marshall
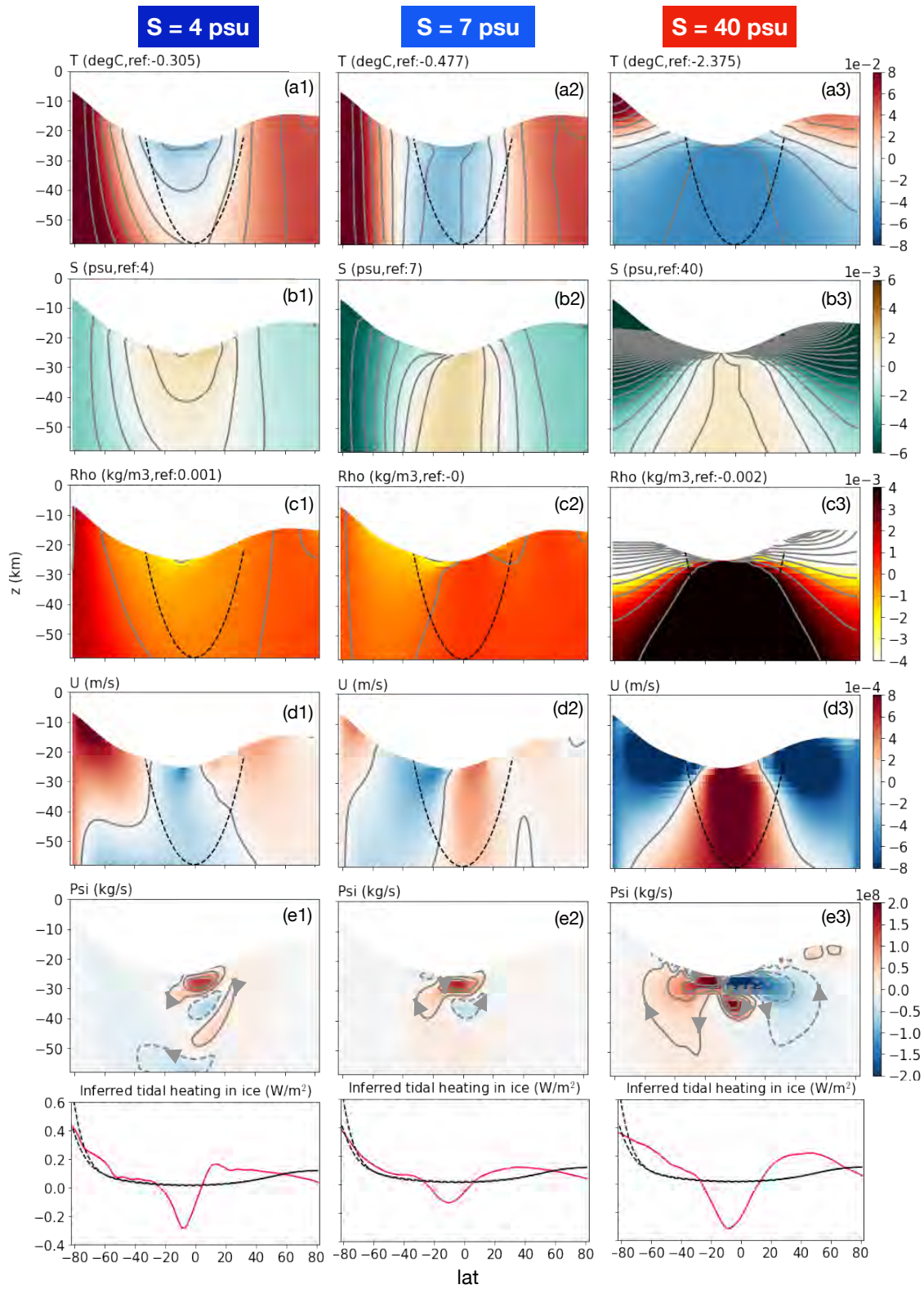
Fig. S9. The sensitivity of the 100% shell-heating scenario solution to lower ice viscosity ($\eta_m = 2 \times 10^{13}$ Pa·s instead of 10^{14} Pa·s), set out as in Fig. S5. Default ocean mixing parameters are used.

is several orders of magnitude smaller than the range explored by *Lobo et al. 2021* (10), which was presumably motivated by those typical of Earth's ocean. Furthermore, in order to sustain the observed ice geometry (4), we argue that the freezing/melting rate is a few kilometers per million years. This can be converted to a buoyancy flux by multiplying the haline contract coefficient β_S, ocean mean salinity S_0 and gravity g. Substituting parameters appropriate to Enceladus yields a buoyancy flux of the order of 10^{-13} m^2/s^3. This is a full 3-6 orders of magnitude smaller than that used in *Lobo et al. 2021* (10). Due to these differences, we prefer not to make quantitative comparison with *Lobo et al. 2021* (10).

References

1. MITgcm-group, MITgcm User Manual, (MIT/EAPS, Cambridge, MA 02139, USA), Online documentation (2010).

2. J Marshall, A Adcroft, C Hill, L Perelman, C Heisey, A finite-volume, incompressible Navier Stokes model for studies of the ocean on parallel computers. *J. Geophys. Res.* **102**, 5,753–5,766 (1997).

3. M Losch, Modeling ice shelf cavities in a z coordinate ocean general circulation model. *J. Geophys. Res.* **113**, 10.1029/2007JC004368 (2008).

4. DJ Hemingway, T Mittal, Enceladus's ice shell structure as a window on internal heat production. *Icarus* **332**, 111–131 (2019).

5. J Rekier, A Trinh, S Triana, V Dehant, Internal energy dissipation in enceladus's subsurface ocean from tides and libration and the role of inertial waves. *J. Geophys. Res. Planets* **124**, 2198–2212 (2019).

6. C Wunsch, R Ferrari, Vertical mixing, energy and thegeneral circulation of the oceans. *Ann. Rev. Fluid Mech.* **36**, 281–314 (2004).

7. MH Redi, Oceanic isopycnal mixing by coordinate rotation. *J. Phys. Ocean.* **12**, 1154–1158 (1982).

8. PR Gent, JC Mcwilliams, Isopycnal mixing in ocean circulation models. *J. Phys. Oceanogr.* **20**, 150–155 (1990).

9. M Visbeck, J Marshall, T Haine, M Spall, Specification of eddy transfer coefficients in coarse-resolution ocean circulation models. *J. Phys. Ocean.* **27**, 381–402 (1997).

10. AH Lobo, AF Thompson, SD Vance, S Tharimena, A pole-to-equator ocean overturning circulation on enceladus. *Nat. Geosci.*, 1–5 (2021).

11. TJ McDougall, PM Barker, Getting started with teos-10 and the gibbs seawater (gsw) oceanographic toolbox. *SCOR/IAPSO WG* **127**, 1–28 (2011).

12. TJ McDougall, DR Jackett, DG Wright, R Feistel, Accurate and Computationally Efficient Algorithms for Potential Temperature and Density of Seawater. *J. Atmospheric Ocean. Technol.* **20**, 730–741 (2003).

13. Chen, E M A, Nimmo, F, Obliquity tides do not significantly heat Enceladus. *Icarus* **214**, 779–781 (2011).

14. M Beuthe, Crustal control of dissipative ocean tides in Enceladus and other icy moons. *Icarus* **280**, 278–299 (2016).

15. HCFC Hay, I Matsuyama, Nonlinear tidal dissipation in the subsurface oceans of Enceladus and other icy satellites. *Icarus* **319**, 68–85 (2019).

16. M Beuthe, Enceladus's crust as a non-uniform thin shell: Ii tidal dissipation. *Icarus* **332**, 66 – 91 (2019).

17. G Choblet, et al., Powering prolonged hydrothermal activity inside Enceladus. *Nat. Astron.* **1**, 841–847 (2017).

18. W Kang, et al., Differing enceladean ocean circulation and ice shell geometries driven by tidal heating in the ice versus the core. *arXiv preprint arXiv:2008.03764* (2020).

19. Y Ashkenazy, R Sayag, E Tziperman, Dynamics of the global meridional ice flow of Europa's icy shell. *Nat. Astron.* **2**, 43–49 (2018).

20. G Tobie, G Choblet, C Sotin, Tidally heated convection: Constraints on Europa's ice shell thickness. *J. Geophys. Res - Atmospheres* **108**, 219 (2003).

21. W Kang, G Flierl, Spontaneous formation of geysers at only one pole on enceladus's ice shell. *PNAS* **117**, 14764–14768 (2020).

22. C McCarthy, RF Cooper, Tidal dissipation in creeping ice and the thermal evolution of Europa. *Earth Planet. Sci. Lett.* **443**, 185–194 (2016).

23. JP Renaud, WG Henning, Increased Tidal Dissipation Using Advanced Rheological Models: Implications for Io and Tidally Active Exoplanets. *Astrophys. J.* **857**, 98 (2018).

24. K Hand, C Chyba, Empirical constraints on the salinity of the europan ocean and implications for a thin ice shell. *Icarus* **189**, 424–438 (2007).

25. V Petrenko, R Whitworth, *Physics of Ice.* (OUP Oxford), (1999).

26. Y Zeng, MF Jansen, Ocean circulation on enceladus with a high versus low salinity ocean. *arXiv preprint arXiv:2101.10530* (2021).
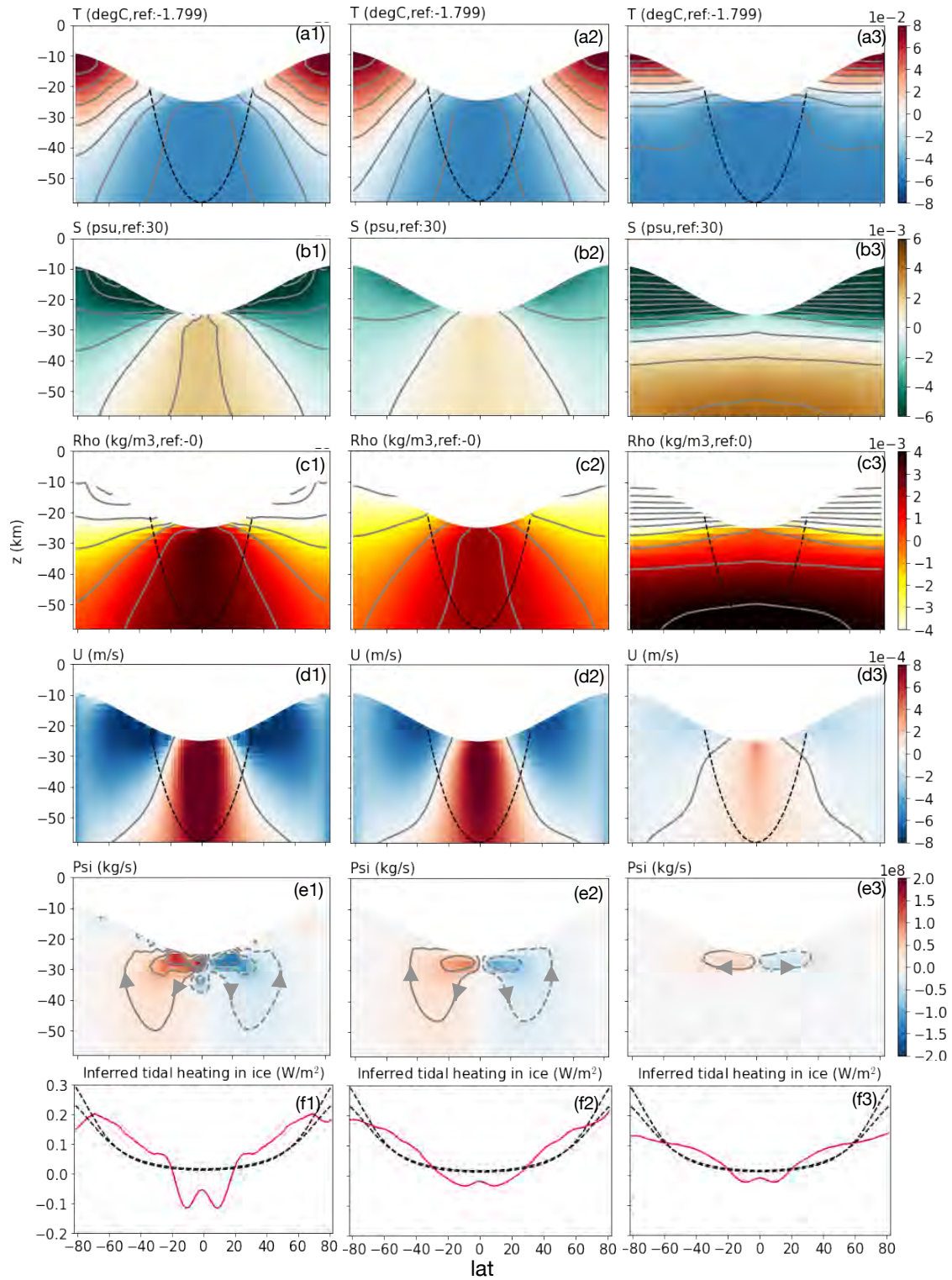
Fig. S10. Solutions under hemispherically-symmetric forcing with the mean salinity set to 30 psu. The left column shows results for default diffusivities ($\kappa_{\mathrm{GM}} = 0.1$ m^2/s, $\kappa_v = \kappa_h = 5 \times 10^{-3}$ m^2/s), the middle column sets the GM diffusivity to zero ($\kappa_{\mathrm{GM}} = 0$ m^2/s, $\kappa_v = \kappa_h = 5 \times 10^{-3}$ m^2/s), and the right column reduces ocean mixing coefficients ($\kappa_{\mathrm{GM}} = 0$ m^2/s, $\kappa_v = \kappa_h = 10^{-3}$ m^2/s).